ULTRAFAST ELECTRON DIFFRACTION ON THE CHARGE DENSITY WAVE COMPOUND $4H_b$-$TaSe_2$

by

Ilana Boshoff

Thesis presented in partial fulfillment of the requirements for the degree of Masters of Science

at

Stellenbosch University

Department of Physics

Faculty of Science

Supervisor: Prof. Heinrich Schwoerer

Co-supervisor: Prof. Erich Rohwer

Date: March 2012

Declaration

By submitting this thesis electronically, I declare that the entirety of the work contained therein is my own, original work, that I am the sole author thereof (save to the extent explicitly otherwise stated), that reproduction and publication thereof by Stellenbosch University will not infringe any third party rights and that I have not previously in its entirety or in part submitted it for obtaining any qualification.

March 2012

Abstract

Ultrafast electron diffraction is a powerful method to study atomic movement in crystals on sub-picosecond timescales. This thesis consists of three parts. In part one the ultrafast electron diffraction machine is described, followed by improvements that were made and techniques that were developed in order to bring the system to state of the art level and enable the acquisition of sufficient data to obtain information on the structural dynamics in crystals. The second part contains a description of the sample which was studied in our first time-resolved measurements, the transition-metal dichalcogenide $4H_b$-$TaSe_2$. This particular crystal is an example of a strongly coupled electronic system which develops a charge density wave (CDW) accompanied by a periodic lattice distortion (PLD). An overview of the formation of electron diffraction patterns and what can be learned from them are also given, followed by the results of the ultrafast electron diffraction experiments done with $4H_b$-$TaSe_2$. Part three describes an alternative source to study dynamics in crystalline samples, namely laser plasma-based ultrafast X-ray diffraction.

The ultrafast electron diffraction group functions as a unit, but my tasks ranged from sample preparation and characterisation of the electron beam to the setting up and execution of experiments. I was involved in analysing the data and contributed small parts to the data analysis software.

Opsomming

Ultravinnige elektron diffraksie is a metode om die beweging van atome in kristalle op sub-pikosekonde tydskale te bestudeer. Hierdie tesis bestaan uit drie dele. In deel een van die tesis word die ultravinnige elektron diffraksie masjien beskryf, gevolg deur verbeteringe wat aangebring is en tegnieke wat ontwikkel is om die sisteem tot op 'n wêreldklas vlak te bring waar die insameling van genoegsame data om inligting oor die strukturele dinamika in kristalle te bekom, moontlik is. Die tweede deel bevat 'n beskrywing van die monster wat in ons eerste tydopgeloste eksperimente gebruik is, naamlik die oorgangsmetaal-dichalkogenied $4H_b$-$TaSe_2$. Hierdie kristal is 'n voorbeeld van 'n sterk gekoppelde elektroniese sisteem wat 'n ladingsdigtheid-golf en 'n gepaardgaande periodiese versteuring van die kristalrooster ontwikkel. 'n Oorsig van die formasie van elektron diffraksiepatrone en wat ons daaruit kan leer word ook gegee. Daarna word die resultate van die ultravinnige elektron diffraksie eksperimente wat op $4H_b$-$TaSe_2$uitgevoer is beskryf en bespreek. In deel drie word 'n alternatiewe metode om die dinamika in kristalmonsters te bestudeer, naamlik laser plasma-gebaseerde ultravinnige X-straal diffraksie, beskryf.

Die ultravinnige elektron diffraksie groep funksioneer as 'n eenheid, maar my verantwoordelikhede het gestrek van die voorbereiding van monsters en die karakterisering van die elektron bundel tot die opstel en uitvoer van eksperimente. Ek was ook betrokke by die analisering van data en het dele van die data analise sagteware geskryf.

Acknowledgements

I want to thank my supervisor, Professor Heinrich Schwoerer, for all the time, effort, passion and support he put into this project, always being willing to give guidance and advice.

To the members of the UED-group, Kerstin Haupt, Nicolas Erasmus and Günther Kassier - thank you for your help, input, motivation and inspiration. I learned so much from each one of you and I really enjoyed working with you.

Also to all the other students in the Kudulab, it was a pleasure to share the laboratory with you.

A big thanks to everyone in the Physics Department, especially Uli Deutschländer, Bull Botha and Eben Shields for their technical skills and support.

A special word of thanks to Mohamed Jaffer from UCT for his help and patience with the sample preparation.

Thank you to Professor Helmut Zacharias and his research group in Münster for having me.

Lastly I want to thank my Lord and Saviour Jesus Christ. Without You none of this would ever have been possible.

Contents

List of Figures

List of Tables

1 INTRODUCTION

Diffraction methods have been used for decades to determine the structure of matter on an atomic scale. This concept relies on the constructive scattering of waves off regular structures to form an angular diffraction pattern from which the arrangement of the atoms can be determined. In order for scattering to take place, particle waves with a de Broglie wavelength ($\lambda = \frac{h}{p}$) comparable to the atomic spacing in a molecule (in the region of 1 Å) are required. Likewise, electromagnetic radiation with an appropriate wavelength (meaning X-rays) is needed. Diffraction was first observed in 1912 when it was discovered that X-rays are diffracted off crystals [1]. The demonstration of electron diffraction followed in 1927 [2] and finally neutron diffraction in 1945 [3].

X-rays are a powerful tool to determine the atomic structure of big molecules, even biological molecules if they can be crystallised [4]. They are scattered by electrons, interacting with the electron cloud which surrounds the nucleus. Their large penetration depth makes them suitable for volume samples, although damage induced by X-rays often limits the lifetime of samples, and crystalline specimens are required. Electrons have a much stronger interaction with matter and a scattering cross section which is 5 orders of magnitude larger than that of X-rays. They are ideal for the investigation of thin targets and surfaces. Neutrons interact with the nucleus of an atom. They are non-destructive and that makes them a perfect probe for materials that require a deep penetration depth (μm − cm) but which are otherwise destroyed by X-rays. They also have a magnetic dipole moment and can therefore be used to determine the microscopic magnetic structure of matter. Until recently these methods could only be used to obtain the static structure of matter. However, what is also interesting is to observe the diffraction pattern during a change in the structure, for example after depositing energy into the system. Dynamic processes like the propagation of phonons [5], heating and melting of lattices [6], structural phase transitions [7] and even strongly coupled electron systems [8] have been investigated using ultrafast diffraction techniques.

In order to directly observe these structural dynamics, spatial resolution better than 1 Ångström ($1\,\text{Å} = 10^{-10}\,\text{m}$) and temporal resolution in the order of 100 femtoseconds ($100\,\text{fs} = 10^{-13}\,\text{s}$) is necessary. To achieve this, traditional diffraction methods are combined with a method used in ultrafast spectroscopy with pulsed laser light, the pump-probe technique. In conventional femtosecond spectroscopy a pump laser pulse induces a reaction in a sample and a delayed probe laser pulse monitors the status of the sample at a particular time after the change produced by the pump pulse. The delay between the two pulses can be varied optically and a measurement of the state of the sample is taken at different delays. This means that the detector can be slow, but the information (for example a series of absorption or transmission spectra) is obtained as a function of time. The temporal resolution is determined by the duration of the pulses and the accuracy of the delay. Due to its wavelength, laser light (visible to extreme UV) can only probe potential energy surfaces and not the structure of matter. So by replacing the light in the probe path with pulsed electrons or X-rays, one can acquire a sequence of diffraction patterns that maps the change of the structure with time. This may sound simple, but the challenge is to produce pulsed X-ray

and electron beams that are short enough to meet the requirements of femtosecond temporal resolution.

Synchrotron facilities are the main sources for X-rays. They are extremely stable, bright and tunable over the infrared to soft X-ray region. However, the minimum pulse duration of synchrotron X-rays is only $10 - 100\,\mathrm{ps}$ which is too long to observe ultrafast structural dynamics. It is possible to produce femtosecond X-ray pulses in a synchrotron through sliced electron beams where a fs laser pulse interacts with the electron bunch, "slicing" out a wedge of electrons which is used to produce fs X-rays, but the flux is very low and long periods of time are needed to gather sufficient data. Free electrons lasers (FEL) are the best source for femtosecond X-rays. They produce a high flux of X-rays (a peak brilliance of $10^{29} - 10^{30}$ photons $\mathrm{s}^{-1}\mathrm{mrad}^{-2}\mathrm{mm}^{-2}$ per 0.1% bw [9]), which are coherent, polarized and has a pulse duration of $10{-}50\,\mathrm{fs}$. In the laboratory, ultra-short X-rays are generated through high harmonic generation (HHG) and by using plasma-based sources. The problem with both these methods is low flux and the fact that X-ray optics are tricky to use and difficult to align.

Ultrafast Electron Diffraction (UED) makes use of table-top laser systems where fs electron pulses are produced through the photoelectric effect by utilising fs laser pulses and high extraction fields. The first UED experiments done on a sub-picosecond time scale observed lattice changes when heating gold [10] and melting metal films like aluminium [6]. After this, photoinduced reactions in small molecules in gas phase were investigated [7] and most recently the structural dynamics in charge density wave compounds like TaS_2 were observed [8]. The complexity of investigated samples is rapidly growing, from pure metals to transient element-chalcogenide charge density wave crystals, but the number of laboratories producing results with a compact UED source is still below ten.

In this thesis the UED setup and the first time resolved experiments that were done at the Laser Research Institute at the University of Stellenbosch is discussed. In Part I the electron diffraction apparatus in our laboratory will be described. The focus will be on the many improvements and changes that were made during my MSc to bring the system up to a standard where the first time resolved measurements can be done. Experiments were performed to investigate the photoinduced destruction of the charge density wave (CDW) in the transition-metal dichalcogenide $4H_b$-$TaSe_2$ and this will be presented in Part II. Charge density waves and their different phases (commensurate, incommensurate and near-commensurate) occur below/between certain well known phase transition temperatures. The dynamics of the structural change which takes place when a sample in the commensurate phase is excited by light was investigated. The recovery time, as well as the dependence on the pump fluence were also examined. In Part III an alternative source to investigate ultrafast structural dynamics, namely a laser plasma-based ultrafast X-ray source, will be explained. This will be based on work done at the Westfälische Wilhelms-Universität Münster, Germany where I spent five months in the research group of Professor Helmut Zacharias.

Ultrafast electron diffraction is in principle a simple and compact, but also a powerful tool which can be used to obtain valuable information about the structural dynamics in crystals on sub-picosecond time scales.

Part I

THE ULTRAFAST ELECTRON DIFFRACTION APPARATUS

In Part I of this thesis I will discuss the setup and properties of the ultrafast electron diffraction (UED) apparatus in our laboratory. Section 2 will give an overview of the key components that make up the UED machine. Understanding how the system works is necessary, but seeing that it has already been described in detail in the MSc thesis of Nicolas Erasmus [11], I will only shortly explain the different components. I will however expand on new elements that were added to the system and not discussed in [11]. The focus of Section 3 will be on developments and improvements made to the setup and characterisations that were done during my MSc to bring our system to a standard which is comparable to the leading UED laboratories in the world.

2 THE ULTRAFAST ELECTRON DIFFRACTION MACHINE

The basic components of an ultrafast electron diffraction system are a femtosecond laser, an optical pump probe setup, an ultrafast electron gun and a detection system. In Figure 2.1 an overview of the UED experiment in our laboratory is shown.

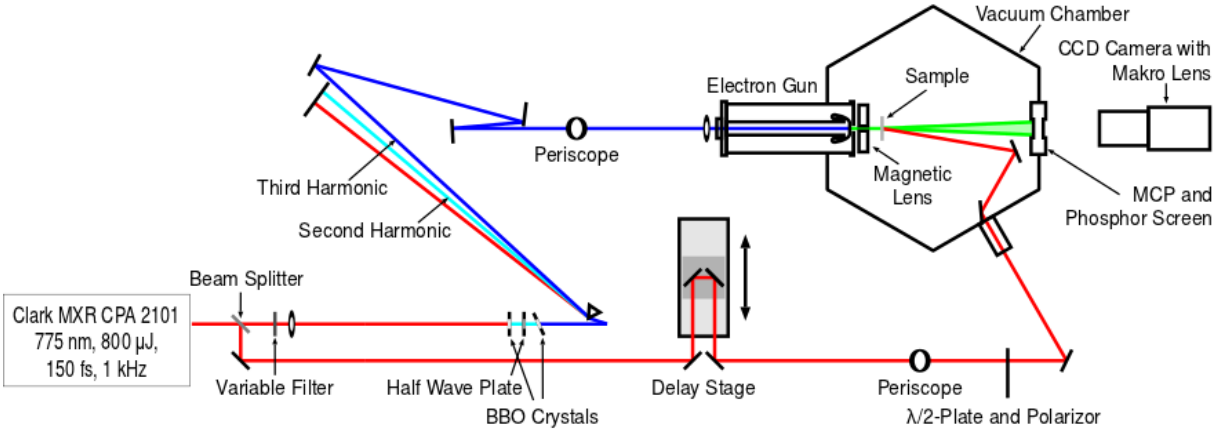

Figure 2.1: This shows an overview of the UED setup in our laboratory. The four main components of the system are a fs laser, an optical pump probe setup, an ultrafast electron gun and a detection system.

Our femtosecond laser source is a *Clark MXR CPA 2101* system which produces 150 fs pulses with an energy of ~800 μJ and a wavelength of 775 nm at a 1 kHz repetition rate. About one third of the power is used for the UED setup, the rest serves the purely optical experiments which can run in parallel. The beam is split into two paths: A pump and a probe path. The pump beam initiates a change in the sample upon illumination and the probe beam is used to produce electron pulses which are diffracted by the sample and monitor the progress of the induced change at certain times after a change is induced by the pump beam.

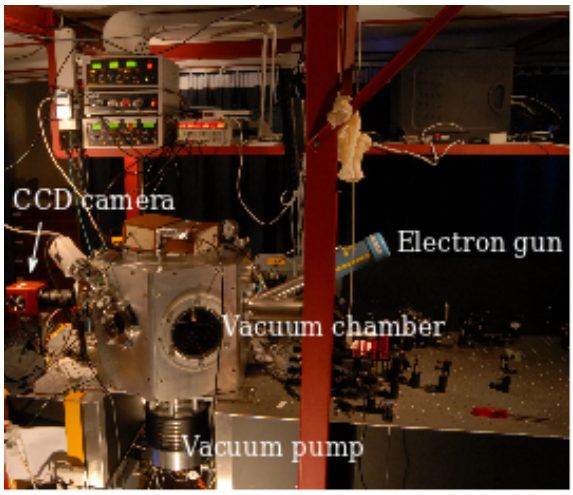

Figure 2.2: The setup in our laboratory. The vacuum chamber, electron gun, vacuum pump and the camera can be seen.

To accomplish this, the optical path length between the pump and probe paths has to be varied. The path length of the pump path is changed using the delay stage (see Figure 2.1) where the beam is reflected 180° by two mirrors mounted on *Zaber RS-232* translation stage with a resolution of 0.5 μm. The constant speed of light means that the time at which the light arrives at the sample can be finely tuned. The delay stage is computer controlled through *LabView* and a move of 1 μm corresponds to a delay of 6.7 fs, keeping in mind that the light has to travel back and forth on the delay stage, see Figure 2.1. Diffraction images are obtained for different delays, resulting in a series of diffraction patterns, tracking the structural change in the sample with time. The beauty of this process is that a slow detector can be used to monitor very fast (~fs) changes in the structure of samples.

In the probe path, electron pulses are produced through the photoelectric effect which states that an electron can be emitted from the surface of matter by light falling onto it. In the electron gun this process is accomplished by shining our laser light onto a photocathode which consists of a quartz window coated with a 10 nm layer of gold (see Figure 2.3). In order to overcome the work function of gold (5.1 eV$\pm$10%, depending on the thickness), the 775 nm light from the laser has to be frequency tripled to 258 nm (4.8 eV). UV light with a spot size of 35 μm and a pulse energy of 110 pJ produces 1 000 electrons. With time this number goes down due to degradation that takes place in the cathode. This is discussed in more detail in Section 3.1 and the characterisation of the electron beam in Section 3.2.

Before the electrons can exit the gun, they need to be accelerated to the required kinetic energy. This is done by an electric field (in the order of 10 kV/mm) which is created by placing a high voltage (variable from $0 - 50$ kV) on the cathode holder and grounding the anode cap. A copper rod is used

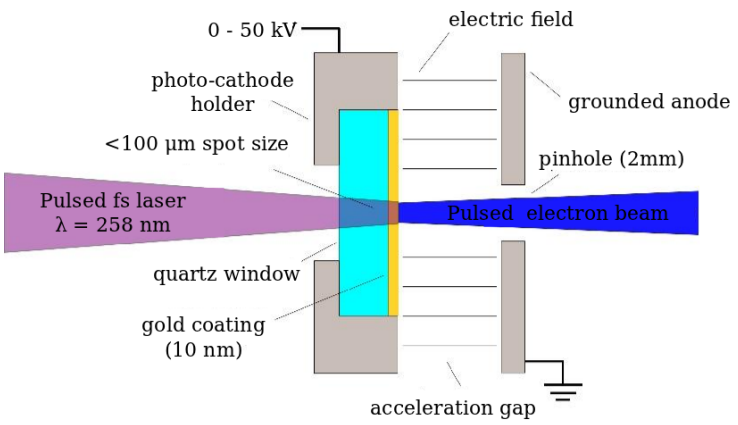

Figure 2.3: UV light is focused onto the photocathode. Electrons are generated through the photoelectric effect and accelerated by a strong electric field.

to put the high voltage on the cathode which is only supported by a macor tube which insulates it from the rest of the gun. A Rogowski profiled holder was chosen to contain the cathode[1] because the shape minimises the chance of discharge and ensures a uniform electric field which is necessary to ensure that all the electrons experience the same force during acceleration. The electrons are extracted through a hole, which has a diameter of 2 mm, in the anode cap and focused by a magnetic lens. The magnetic lens basically consists of a casing with high magnetic permeability which has coiled wires on the inside. The electrons travel through a hole in the casing (around which the wires are wrapped) and when a current is passed through the wires, the electrons experience the magnetic field which alters their direction of propagation and focuses the electron beam. By varying the current through the wires, the electron beam can be focused onto different positions. At the sample, the electron beam has a diameter of less than 400 μm (see Section 3.2 for more information). Also remember that before an experiment can be done, spatial and temporal overlap between the pump and probe pulses have to be obtained and the methods are explained in Section 3.3.

Electrons with an energy of 30 keV have a mean free path of only 1.5 cm in air [12]. Due to this fact, experiments have to take place in vacuum. The chamber is pumped by a *Oerlikon Turbovac SL 700* turbomolecular pump which is connected to an *Adixen 2015SD* rotary-vane pump with a valve in between. The electron gun is pumped by a separate turbo pump (*Leybold TW70H*) to ensure that a good vacuum is also obtained inside the electron gun. A pressure of 5×10^{-6} mbar is reached after a day of pumping.

A sample, mounted on a *Micos* xyz-translation stage to ensure optimal mobility inside the chamber, diffracts the electrons. The preparation of thin samples (a thickness of less than 100 nm is necessary for ultrafast electron diffraction in transmission geometry) is described in Section 3.6. The electrons pulse broadens due to Coulomb repulsion between the electrons and to keep the duration of the electron pulse as short as possible, the propagation distance of the electrons must be minimised by placing the sample as close as possible to the cathode. We measure the electron pulse duration with our streak camera [13], as described in Section 3.2. The diffracted electrons are detected and amplified by secondary electron

[1] This choice was based on simulations done by PhD student Kerstin Haupt, testing various different configurations.

emission in micro channel plates (MCP's) and accelerated onto a phosphor screen. The system consists of two MCP plates (*Tectra MCP 050*) in Chevron configuration, a 40 : 1 ratio (channel length:diameter), a 12 μm pore diameter and a 15 μm centre to centre distance. For double MCP's, the expected gain is 5×10^6 at 2 000 V (1 000 V per MCP). We typically supply our system with 4.4 kV of which 0.7 kV goes to each respective MCP and 3 kV to the phosphor screen for the acceleration of the electrons. When the electrons hit the phosphor screen, photons are emitted and the light is captured by a 60 mm macros lens which images it onto a Peltier cooled CCD camera (*EHD SC4022*) to obtain a diffraction image. The properties of the camera are covered in Section 3.5.

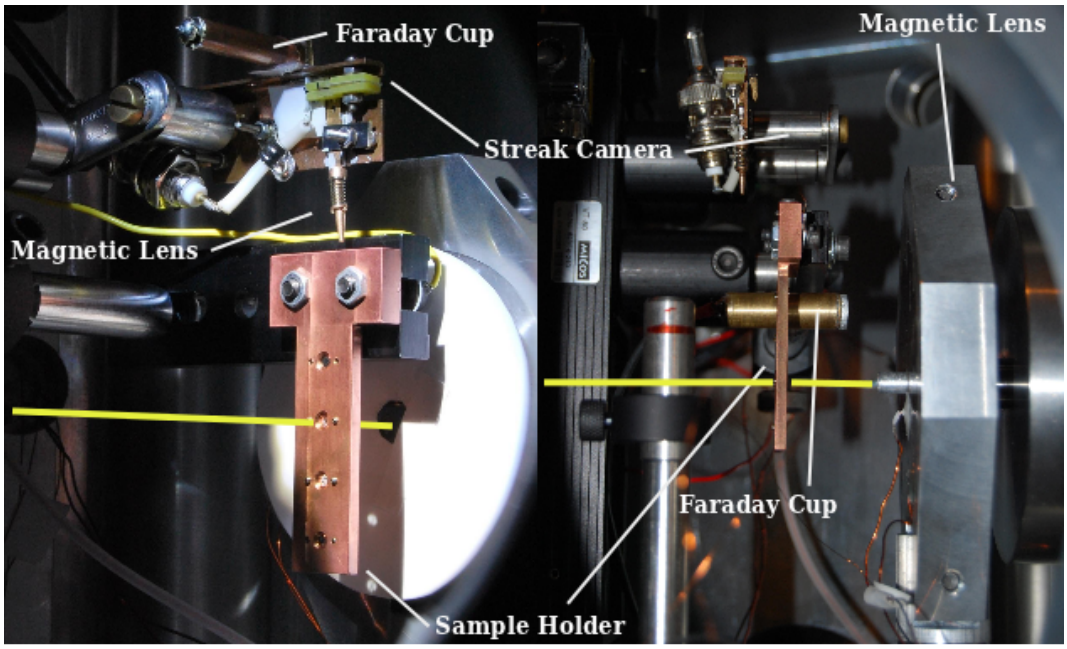

Figure 2.4: The inside of the vacuum chamber shown from different angles. The magnetic lens and the sample holder can be seen, as well as the streak camera and the Faraday cup which are respectively used to measure the electron pulse duration and determine the number of electrons per pulse, as discussed in Section 3.2. The yellow lines indicate the path of the electrons in a diffraction experiment.

The objective of this setup is to obtain information on the structural dynamics in crystals on a sub-picosecond timescale with Angström spatial resolution, but to acquire sufficient data using the UED machine can take up to 20 hours (a short description of the process is given in Section 3.7). Getting to the point where we were able to run experiments over such long periods of time meant that a lot of improvements had to be made to the system and these, as well as the characterisation of the machine, are discussed in the next section.

3 IMPROVEMENTS TO AND CHARACTERISATION OF THE UED MACHINE

Before an ultrafast electron diffraction experiment can be executed, there are many things which need to be taken into consideration, such as the characterisation of the system, ensuring that the setup is stable over the course of a measurement and the preparation of the samples which are to be investigated. In this section I will discuss the changes and improvements made to the UED setup and expand on challenges and requirements to run a successful ultrafast electron diffraction experiment, which means a constant performance from the system over several hours and acquiring diffraction patterns which are good enough so that useful information can be extracted from them

3.1 PHOTOCATHODE: PERFORMANCE AND DEGRADATION

The photocathode consists of a quartz window (3 mm thick) coated by a 10 nm layer of gold which is where electron pulses are generated through the photoelectric effect. It is an essential part of the system, but currently it is the weakest point in our setup. A typical experiment runs over up to 20 hours, but we have not yet found conditions under which the photocathode performs stably over several hours. The electron number decreases with time due to an unidentified ageing process. The signal strength (the integrated intensity over a particular Bragg reflection) is tracked over the course of an experiment and we typically see a drop of 50% over 20 hours (see Figure 3.1). It is possible to improve the signal by moving the UV spot on the cathode, but one have to take care that nothing else (such as the spatial and temporal overlap, discussed in Section 3.3) runs out of alignment. A possible reason for this decay can be that the vacuum, being $> 10^{-6}$ mbar, is not good enough and the presence of oil in the chamber leads to the surface deposition of aromatic molecules on the cathode. If the UV light excites these molecules, some of the absorbed energy is transferred into heat, which might alter or damage the gold layer. Another hint towards surface deposition is the fact that pre-irradiation of the cathode with low intensity UV light improves the lifetime of the cathode, probably by removal of surface contaminants.

Due to the fact that experiments need such a long period of time to complete, one might argue that the conditions (temperature and humidity) in the laboratory will not be stable and that will have an impact on the laser which will have an effect on the electron source. The laboratory environment is continually measured and typical results are shown in Figure 3.2. Over the course of almost 40 hours, there is only a change of 0.5°C in the temperature and a 5% fluctuation in the humidity. The output of the *CPA2101* is also constantly monitored behind a back polished mirror, just after the laser output window on a 1 μJ level, and calibrated against a full power reading. A detector (*Thorlabs S120C* photo diode, *PM100A USB* interface, controlled by *LabView*) takes a measurement every 10 seconds. The result (see Figure 3.3) is an output pulse energy (kept constant at 730 μJ) which is stable within 1% over 28 hours. From this we can conclude that neither the conditions in the laboratory, nor the performance of our laser are the cause

of the degradation in our electron beam. When moving the UV beam around on the cathode, one can observe the electron beam getting dimmer at certain positions. This points to the fact that degradation takes place on the cathode itself and that is what causes a drop in the number of electrons which are produced by UV pulses with a certain energy.

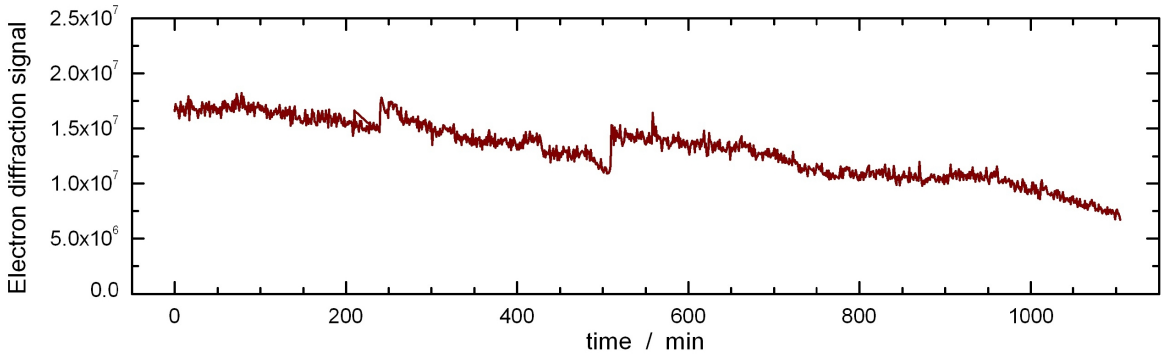

Figure 3.1: The electron intensity of a particular Bragg reflection is monitored over the course of a measurement. Typically a drop of 50% occurs over this period of time. Jumps in the signal are due to moving the UV beam onto a fresh spot on the cathode in order to enhance the signal.

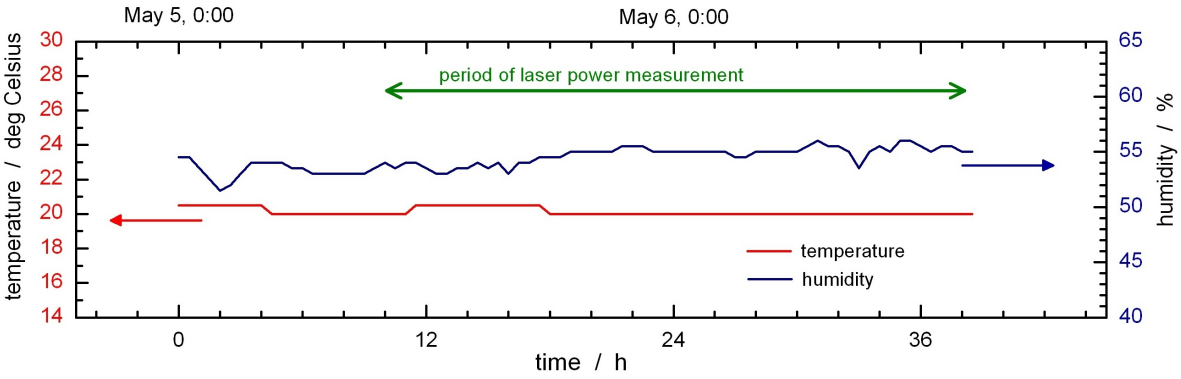

Figure 3.2: The conditions in the laboratory, tracked over a period of nearly 40 hours. The temperature (red line) is practically constant at 20°C, there is only a change of 0.5°C, while the humidity (blue line) fluctuates by less than 5 %. Due to the fact that the conditions in the laboratory are so stable, the degradation of the cathode most likely occurs because of a process in the cathode itself.

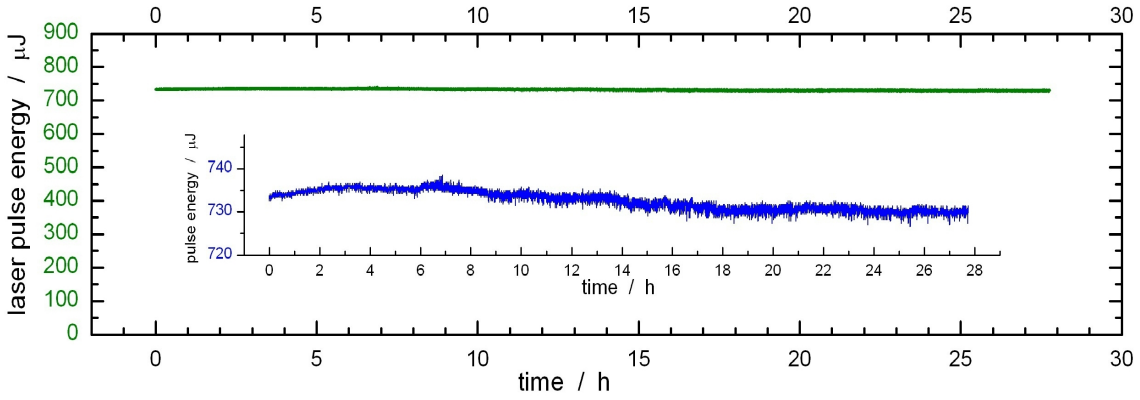

Figure 3.3: The output energy of the laser over a duration of 28 hours. On the green scale it seems to be perfectly constant at 730 μJ. On the blue scale it can be seen that there are some small fluctuations, but the energy is still stable within 1%.

We have varied the pulse energy and intensity of the UV beam in an attempt to find suitable illumination conditions and have found obvious, but not quantifiable, dependence on both parameters. Because we apply a linear photoionisation, the number of electrons only depends on the pulse energy. This means that for higher energies (more electrons) the signal strength and signal to noise ratio of the diffraction pattern is better, but the rate of decay of the cathode is faster and at the same time one also has to keep the electron pulse duration, see Section 3.2, in mind. On the other hand, the diffraction pattern is improved by reducing the electron source size, meaning the size of the UV spot on the cathode (see Figure 3.6 in Section 3.2). This is due to higher transversal emittance, but implies a higher illumination intensity. Typically experiments are done with a UV pulse energy of 70 pJ and the spot size of the UV beam on the cathode, if it is in focus, is 35 μm. At a pulse duration of 150 fs, this corresponds to an intensity of 1.2×10^7 W/cm^2 on the surface of the cathode.

A significant improvement was achieved by reducing the thickness of the gold layer from 25 nm to 10 nm. The mean free path of an electron with an energy of 5 eV in gold is very small, which means that by making the gold layer thinner, the efficiency of the cathode is improved because fewer electrons are lost and with less UV pulse energy the same number of electrons can be generated.

Additionally a number of different things were investigated in an attempt to improve the performance of the cathode. A sapphire (instead of quartz) window was used because of the lower absorption in the UV, but this made no observable difference. We also made use of a platinum coated cathode for the reason that platinum has a higher melting point and work function than gold which would require more UV pulse energy, but should improve the beam quality. However, there was no obvious change in the degradation of the cathode.

In order to improve the vacuum inside the electron gun, a separate vacuum pump (*Leybold TW70H*) was attached to the gun. This, in combination with pre-irradiating the cathode for 30 minutes at a low

UV intensity, enabled the use of a UV pulse energy which was four times higher, but displayed the same rate of decay as the lower UV energy without pre-illumination of the cathode.

In the future either the performance of the cathode will have to be improved or the duration of an experiment reduced. Another option is to build a moving or rotating cathode, but in the mean time the number of electrons which is produced can be recovered by moving the UV spot on the cathode.

3.2 CHARACTERISING THE ELECTRON BEAM

The characterisation of the electron beam in an ultrafast electron diffraction experiment is very important, as it effects the spatial overlap and the spatial and temporal resolution of the measurement. Parameters which need to be determined are the number of electrons per pulse, the size of the electron beam at the sample and the duration of each electron pulse. The beam size needs to be small enough to obtain spatial overlap and the pulse duration (which is directly related to the number of electrons) has to be short enough to give a sub-picosecond temporal resolution. Special techniques are required to determine each of these parameters and these methods will be discussed in this section.

Number of Electrons per Pulse

An important measurement to characterise the electron beam, is the determination of the number of electrons per pulse. The pulse duration (discussed on page 14) depends primarily on the number of electrons per pulse and therefore it is a very important parameter for the temporal resolution of the experiments. As mentioned in Section 2, electrons are generated through the photoelectric effect by shining UV light onto a photocathode. This is a linear process which means that each electron is produced by a single photon, but a single photon can only produce an electron if it has sufficient energy. Additionally one can conclude that the number of electrons can be determined as a function of the UV power.

A UV photon with a wavelength of $\lambda = 258\,\text{nm}$ has an energy of $7.698 \times 10^{-19}\,\text{J}$ ($E = h\nu = \frac{hc}{\lambda}$). Using this value, the number of photons per pulse can be determined from the pulse energy. Similarly each electron has a charge of $e = 1.602 \times 10^{-19}\,\text{C}$ which can be used to calculated the number of electrons per pulse from a current measurement.

The UV power is measured by a *Thorlabs S120VC* power meter, but this instrument is only sensitive down to $0.1\,\mu\text{W}$. This corresponds to an energy of 0.1 nJ per pulse, because 1 W=1 J/s and the repetition rate of the laser is 1 kHz, but it is often necessary to work at even lower pulse energies (in the order of pJ).

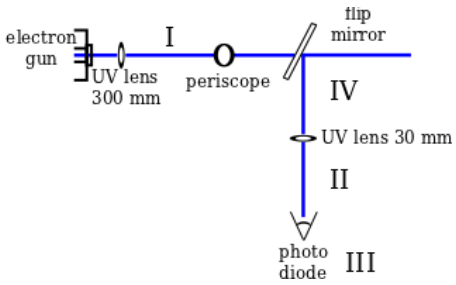

Figure 3.4: The setup to measure the UV pulse energy using a photo diode. It is directly proportional to the number of electrons which are generated.

To measure these low energies, a UV sensitive photo diode (*Thorlabs Det10A/M Si biased detector* which is sensitive to light in the 200–1100 nm range) is used to determine the pulse energy. The photo diode measures a voltage (V) and the power meter, which gives an absolute value, is used to calibrate the photo diode at higher pulse energies and then the photo diode can be used to determine the lower pulse energies. The UV light is reflected onto the photo diode using a flip mirror, which makes it very quick and easy to measure the pulse energy and determine the corresponding number of electrons before running an experiment, assuming constant conditions of the photo cathode. The setup is shown in Figure 3.4 and the results are listed in Table 3.1. We found that 100 mV measured with the photo diode indicates a pulse energy of 70 pJ.

Table 3.1: The calibration of the photo diode to determine the UV pulse energy. 100 mV measured with the photo diode at position III (see Figure 3.4) corresponds to a pulse energy of 70 pJ on the photocathode.

	Power (μW)			Energy/pulse (nJ)		Voltage (V)
Position	I	II	IV	II	IV	III
	3.0	3.0				
		0.18	0.21	0.18	0.21	0.21
		0.75	0.93	0.75	0.93	1.10

The electron current is measured using a Faraday Cup, which is a simple device used to determine the amount of charged particles in a beam in vacuum. It is basically a metal cup which catches charged particles (electrons in our case) and as they hit the metal it gains a small net charge. By grounding the cup it can be discharged and the current can be measured. The current is measured by a *Keithley 6487 picoammeter* which is sensitive to currents as small as 10 fA. Keep in mind that measured current is the amount of charge that passes a certain point per second and that our laser has a frequency of f = 1 kHz and therefore $N_{electrons/pulse} = \frac{I}{e\,f}$. The results are given in Table 3.2 and in Figure 3.5 the linear dependence of the number of electrons on the UV power can be seen.

These measurements were done before the start of an experiment meaning that the laser was focused onto a fresh spot on the cathode (see Section 3.1 for a discussion of the degradation of the photocathode). During an experiment the electron flux goes down and typically the electron current, corresponding to a UV pulse energy of 112 pJ, drops from 0.16 pA (1 000 electrons per pulse) to 0.10 pA (624 electrons per pulse) which is a decay of almost 40 % in the efficiency of the cathode. As the number of electrons go down, the electron pulse duration becomes shorter. This means that the temporal resolution of the experiment is not compromised, but the signal to noise ratio becomes smaller and the result is that more data needs to be acquired.

Table 3.2: Measurements to determine the UV pulse energy and the corresponding number of electrons per pulse. The smallest current (0.03 pA) lies on the border of the sensitivity of the ammeter, but in such cases the number of electrons corresponding to the UV pulse energy can be determined from the linearity between the UV pulse energy and the number of electrons per pulse, as shown in Figure 3.5.

UV Voltage (mV)	UV energy/pulse (pJ)	Number of photons/pulse	Current (pA)	Number of electrons/pulse
38	27	3.51×10^{7}	0.03	187
160	112	1.45×10^{8}	0.16	999
850	595	7.73×10^{8}	0.92	5 743
2900	2030	2.65×10^{9}	3.7	23 096

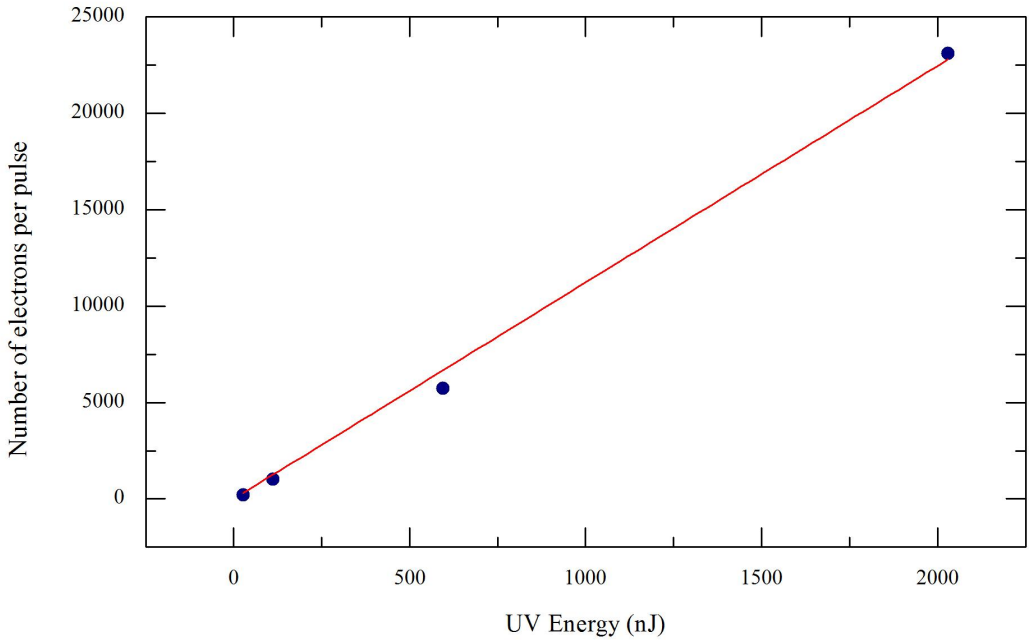

Figure 3.5: The linear dependence of the number of electrons on the UV pulse energy. The lowest current measurement lies on the edge of the sensitivity of the ammeter, but even for very low currents the number of electrons can be determined from its linear relationship with the UV pulse energy. The slope of the line is 11.7 electrons per pulse per nJ.

Electron Beam Size

As the electron beam propagates through space, it is spread out as a result of Coulomb repulsion. The electrons are also focused by a magnetic lens and therefore the diameter of the electron beam at the sample is different to that of the UV beam on the cathode and the electron beam on the phosphor screen. This means that the electron beam size cannot be determined by simply using the spot size on the phosphor screen, but it is necessary to know the size of the electron beam at the sample in order to ensure spatial overlap (see Section 3.3) between the laser pump and the electron probe pulses.

A rough technique to determine the beam size at the sample, is to simply move an aperture (with a known diameter) across the beam and see how many steps on the translation stage (1 step = 2.5 μm) are needed to pass the entire beam. This can only be used to estimate the beam size and a more precise method is necessary to determine the actual beam size. It is done by moving a sharp edge (mounted in the same plane as the sample) across the beam and the integrated intensity is plotted as a function of the scanning distance. By fitting a function to the data and taking the derivative of the curve, the electron beam profile can be calculated. The function ons has to fit depends on the shape of the beam, say if it is a spatially Gaussian beam or a flattop beam. For this reason the interpretation of the result of the shadow intensity measurement depends on an assumption. To improve this, one can move the edge across the electron beam in both the vertical and horizontal directions. The diameter of the electron beam does depend on the number of electrons, but under typical experimental conditions the beam diameter is always less than 400 μm.

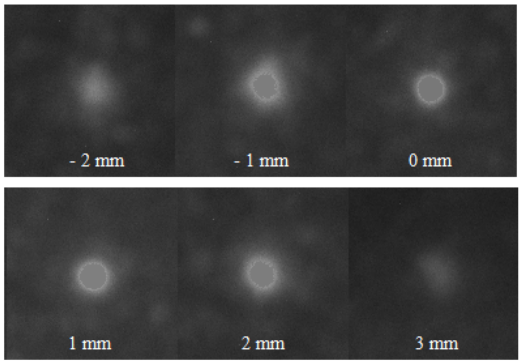

Figure 3.6: A particular Bragg reflection for different positions of the UV focusing lens. The distance indicates how far the focus of the UV beam is from the cathode. At 0 mm we see that the beam is sharper and more intense.

The UV beam also influences the electron beam's size and quality in terms of spatial coherence and energy spread. Not only does the initial size of the electron beam depend on the size of the UV spot on the cathode, but it also has an effect on the quality of the diffraction pattern. This is illustrated in Figure 3.6 where a particular Bragg reflection is shown for different sizes of the UV beam on the cathode. At the position where the cathode is in the focus of the UV light, the Bragg reflection has the smallest, brightest and sharpest appearance, but keep in mind that if the space charge is too high the coherence is lost.

Electron Pulse Duration

The temporal resolution of a pump-probe experiment is limited to the pulse duration of the pump and probe pulses and therefore it is essential to determine how long (temporally) these pulses are. Measuring the duration of a femtosecond laser pulse is a standard procedure. We measure the pulse duration of the first harmonic and conservatively assume that the third harmonic has the same duration. At the instance of generation, the electron pulse has the same duration as the laser pulse used to generate it, but due to space charge effects (the Coulomb repulsion between electrons) this changes quickly. According to simulations done by a member of our group, Günther Kassier [14], the pulse duration depends on the number of electrons and how far they have to propagate. This is plotted in Figure 3.7 from which we see that an electron bunch with 2 000 electrons (0.00032 pC) and 30 keV energy will expand to 300 fs after only propagating a distance of 7 cm. In order to obtain a useful diffraction pattern, we need 10^3 electrons per pulse and so the key to having sub-ps electron pulses, is minimising the propagation distance to the sample.

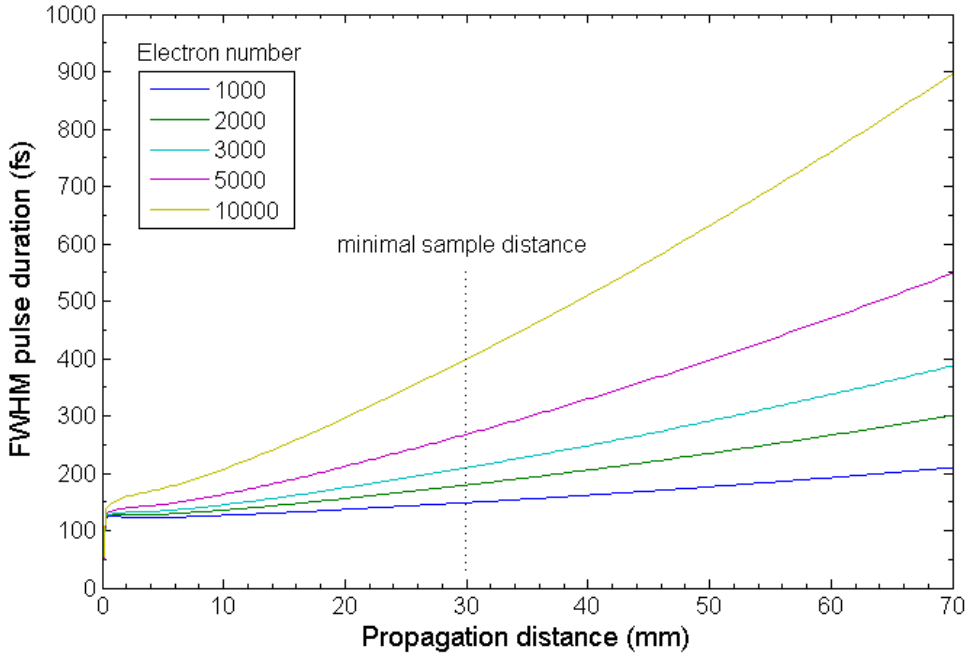

Figure 3.7: The simulation done to show the relation between the number of electrons and the electron pulse duration for electrons with an energy of 30 keV. An initial pulse duration of 120 fs is used.

To measure the duration of an electron pulse, special methods are needed and general techniques include the use of a streak camera and laser ponderomotive scattering [15]. In our setup we make use of a streak camera. The theory, design and characterisation of this streak camera has been described extensively [13, 14] and I will only give a brief description of the basic principle and how it is used to determine the electron pulse duration.

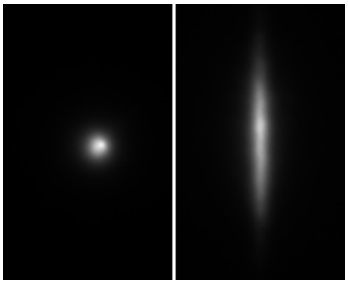

Figure 3.8: An electron spot - unstreaked on the left and streaked on the right.

A streak camera operates on the principle that a rapidly changing (oscillating) electric field is applied to the electrons, perpendicularly to their propagation direction. If the electric field changes fast enough, the electrons at different positions in the pulse experience different field strengths and are deflected at different angles. The result is that the pulse is smeared out and by measuring the length of this streak, the pulse duration can be determined. An example of a laterally streaked pulse is shown in Figure 3.8.

In Figure 3.9 a schematic drawing of the streak camera used in our setup is shown. The main components are an aperture for the electrons (d = 50 μm), the streak plates, the photo switch and the high voltage supply. The streak plates consist of PC board pieces and are only 3 mm long which means that the electrons are only exposed to the electric field for a very short time (30 ps for 30 keV electrons) and the broadening of the pulse due to Coulomb repulsion within the streak camera can be ignored. A pulsed high voltage supply, which is synchronised with the laser, charges the streak plates. Typically a high voltage of ~1 000 V with a duration of 50 ns is applied at a repetition rate of 1 kHz, the same as that of the laser. When the GaAs photo switch is illuminated by the laser pulse, charge carriers are generated in the initially insulating GaAs. The latter becomes conductive, the capacitor is short circuited and starts oscillating. After a quarter of the oscillation period the electric field is zero, but its gradient is maximum and that is where we want to position the electron beam. The electron pulse is streaked by the electric field and from that the pulse duration can be calculated. By varying the optical path length with the delay stage, the calibration of the deflection of the electron bunch vs. time is done and this is referred to as the "streak velocity". The timing between the laser trigger pulse and the electron beam is adjusted to the point where the oscillating electric field goes from negative to positive. This position is found by observing the deflection of the electron spot. Where there is no deflection, the size of the electric field is zero.

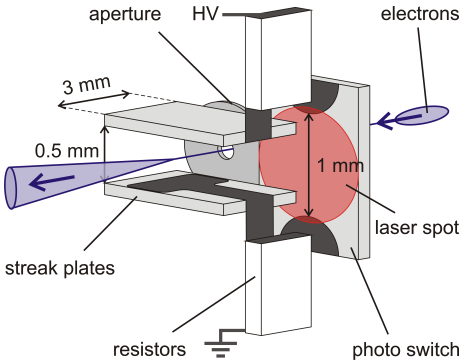

Figure 3.9: The design of the streak camera used in our setup.

3.3 SPATIAL OVERLAP AND TIME ZERO

Before an experiment can be done, there are two very important tasks which need to be completed: obtaining spatial overlap and finding time zero. Spatial overlap occurs when the pump laser pulse and the probe electrons pulse hit the same area on the target and is essential to ensure that the correct area is probed. Time zero refers to the moment when the change is triggered in the sample and it is necessary to know the instance when the pump and probe beams arrive simultaneously. A sophisticated procedure must be in place to assure overlap, since the electron pulse and the laser pulse are counter-propagating with respective speeds of $c/3$ and c and they have to meet within a diameter of 100 μm and a length of 10 μm. Additionally, this has to take place inside a vacuum chamber which means that imaging of the overlap is not possible.

Spatial overlap

Overlapping the pump and probe beams in space is necessary to ensure that the area which is excited by the pump beam and probed by the electrons, is the same to prevent the observation of an area where no change takes place. It is preferable for the pump beam to have a bigger diameter than the probe beam to ensure that a reaction is triggered in the entire area which is probed and that the probe volume ($\sim 5\times10^{-16}$ m^3) is homogeneously illuminated. This is true in our case, but keeping in mind that the diameter of the laser pump beam is 590 μm, the probe beam's is 400 μm and the fact that overlap has to be obtained inside the vacuum chamber, makes this a challenging exercise.

To accomplish spatial overlap, we make use of an aperture (d = 100 μm) which is mounted on the target holder. It is important that the aperture is mounted in the same plane as the samples because the pump and probe beams fall in at slightly different angles and therefore the spatial overlap is very sensitive to position in the propagation direction. First the electron beam is guided through the centre of the aperture. This is done by moving the translation stages and observing the shadow of the target mount on the phosphor screen. The next step is to move the pump beam onto the same aperture by adjusting its path with a piezo mirror which is mounted inside the chamber. The translation stages have a resolution of 2.5 μm and the piezo mirror resolution is $<$1 arcsec. There are white cards placed in strategic positions on the chamber walls to help with the alignment of the pump beam. The back reflection from the aperture falls onto one card and the light which goes through the aperture goes onto a second card. When both the pump and probe beams are aligned through the aperture, spatial overlap is established and one can move on to determining time zero.

Time Zero

Finding the exact moment at which the pump and probe beams arrive at the sample simultaneously is possible because the two pulses originate from the same source, a 150 fs long laser pulse. It is quite

remarkable that we can determine time zero within about hundred femtoseconds when considering the following:

The path length is long - the point where the laser beam is split into a pump path and a probe path is far away from the position where temporal overlap has to be obtained. The pump light travels a distance of more or less 3780 mm to the target. The probe light on the other hand, covers 1120 mm before it undergoes frequency tripling. It then precedes another 2450 mm to the point at which electron pulses are generated. The electron pulses are accelerated over a few millimetres and then they have to advance a final 70 mm before they reach the sample. Also remember that electrons and light travel at different speeds and in opposite direction. An electron with a kinetic energy of 30 keV moves at roughly one third of the speed of light ($E_k = \frac{1}{2}\, mv^2$, $m_e = 9.11 \times 10^{-31}$ kg). This means that a change of 10 μm in the target position will shift time zero by 133.3 fs (40 μm in air and 20 μm on the delay stage) if it moves towards the electron source and 66.7 fs (20 μm in air and 10 μm on the delay stage) if it shifts away from the electron source towards the pump beam. So, due to the difference in speed at which the electrons and light travel, the pump and probe paths have different path lengths.

A rough estimate of time zero is first found by using the streak camera which is mounted directly above the target holder. The concept of the streak camera was explained in Section 3.2 and time zero is found by observing the deflection of the electron beam. It 'oscillates' on the phosphor screen and the position where the oscillation starts indicates time zero. This gives a time window of a few mm on the delay stage (more or less 5 mm which is 33.3 ps) which has to be further refined. To achieve this, the translation stages are moved so that the electron beam passes through an aperture of 100 μm diameter. The pump beam is moved slightly onto the edge of the aperture and then the intensity is increased to form a plasma. As the plasma is formed, the metal aperture is ionised and this repels the electrons and that results in a displacement of the electron beam on the screen. This displacement is a maximum at time zero (when the electrons and the plasma are present at the same time). If the electrons arrive before the plasma is created, there is no movement in the position of the electron beam and the longer they arrive after the formation of the plasma, the less prominent this shift of the electron beam is because of relaxation and charge redistribution in the plasma and the aperture. So time zero is found by determining the position of the delay stage where the electron beam is first displaced. This is illustrated in Figure 3.10.

Initially we produced a visible plasma to find time zero. This resulted in a distortion of the electron beam, but we found that there is enough movement of the beam to determine time zero without generating a plasma that can be seen by the eye, which is good because this also preserves the MCP and phosphor screen (see Section 2). Using this method we can determine temporal overlap within a few picoseconds and then the precise time zero is determined by analysing experimental data. It is remarkable that time zero not only stays stable over the duration of a measurement, but we found that there was less than 100 fs (which corresponds 16.7 μm on the delay stage) change in temporal overlap over the course of weeks if all other parameters, such as the electron energy, remained the same.

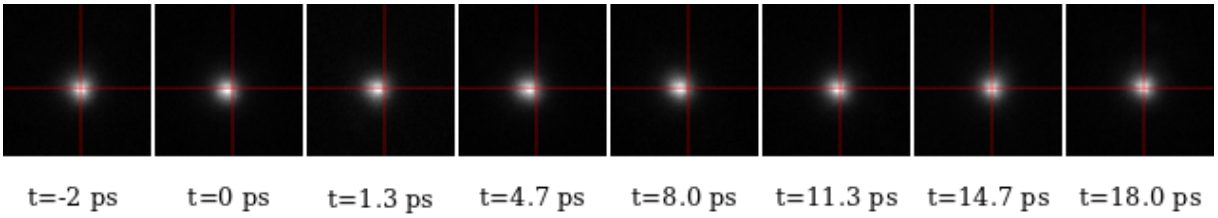

Figure 3.10: The displacement of the electron beam by a plasma (created by shining the pump beam onto an aperture) in order to acquire temporal overlap. At time zero, t = 0 ps, there is a clear shift of the beam to the left and at t = 11.4 ps it starts to recover. At t = 14.7 ps the plasma is gone by the time the electron beam arrives and there is again no displacement.

3.4 BEAM CORRECTION AND STABILITY

As already said, it can take up to 20 hours to complete a measurement. This means that a very stable setup is needed, but no system is perfect over such a long period of time. As discussed in Section 3.1, the conditions in the laboratory do not change remarkably, but it is crucial to ensure that spatial overlap is not lost over the course of a measurement. Additionally we found that the delay stage is unstable at certain positions and that will certainly result in a loss of spatial overlap. To overcome this problem, beam correction was incorporated in both the pump and probe paths in the following manners:

Pump beam

As mentioned above, movement in the pump beam can be due to laser drift, as well as fluctuations in the delay stage. The position of the laser beam on the sample needs to be tracked, but we cannot do this inside the chamber. Therefore the back reflection of the pump beam from the entrance window into the vacuum chamber, is imaged onto a camera which is mounted the same distance from the window as the sample inside the chamber. The result is that any change in position of the pump pulse on the sample will result in an equal change on the camera and this is used to observe the movement of the pump beam. Before starting an experiment, the coordinates of the centre of mass is recorded and stored. After each movement of the delay stage (before obtaining an image at the new time step), the position of the beam is compared to the original. A movement tolerance of 5 pixels is set and if necessary, a piezo mirror moves the beam back to the initial spot. 5 pixels correspond to a distance of 26 μm which is 4.4% of the pump beam size and 6.5% of the diameter of the probe beam. The mirror is calibrated beforehand to determine how the movement of the piezo mirror will affect the position of the laser beam.

Probe beam

Directional change in the electron beam can be controlled making use of the same principle as discussed for the pump beam. It is not possible to adjust the electron optics (the magnetic lens) and therefore we

use a piezo mirror to correct the UV beam just before is enters the electron gun. To track the movement of the electrons, the central electron beam or one of the Bragg reflections in the diffraction pattern on the phosphor screen is monitored. This can be done because if the electrons move on the sample, the whole diffraction pattern will shift. The movement of the electrons is not connected to the movement of the UV in a linear manner, meaning that if the UV beam moves to the left, it does not mean the electron spot on the samples also moves to the left, but in arbitrary direction. Therefore the piezo mirror has to be calibrated to establish the relationship between the UV and electron positions. As with the probe beam, the initial coordinates are logged and at every time step the new position is acquired and, if the set tolerance of 2 pixels is broken, correction takes place before continuing with the experiment. 2 pixels correspond to 14.8 μm on the camera, but a movement of 38 μm of the diffraction pattern on the phosphor screen. The movement of the pump beam is shown in Figure 3.11.

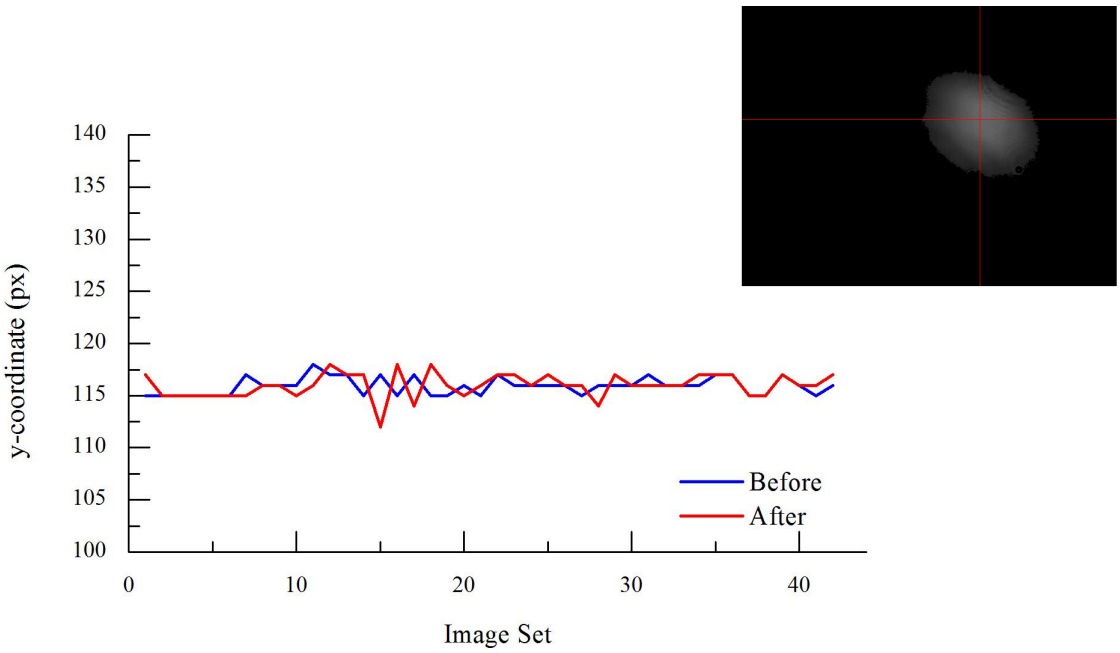

Figure 3.11: This measurement example (from the log file of the experiment programme) shows the movement of the probe beam over the course of a single scan which took more than an hour to complete. The blue line indicates the y-coordinates (in pixels) of the centre of mass of the monitored spot before acquiring pumped and unpumped images and the red line the coordinates afterwards. After obtaining 15 image sets, the alignment was out and the beam correction moved it back to the original coordinate of 115 px. On the right is the image of the pump beam with the red cross indicating the centre of mass. For the pump beam 1 px is equal to 5.2 μm and this corresponds to the actual size or movement of the beam. On the camera monitoring the probe beam 1 px is 7.4 μm and on the phosphor screen it is 19 μm , but this value is not a direct measure of the size of the movement of the probe beam.

3.5 DETECTION AND CAMERA

To improve the detection of the diffraction pattern on the phosphor screen, we replaced our camera, a commercial *Nikon D60,* with a Peltier cooled CCD camera *(EHD SC4022)*. The camera has a chip which contains 2048×2048 pixels and the size of each pixel is $7.4\,\mu$m. The sensor has a diagonal length of 21.4 mm. The biggest improvement however is the fact that the new chip has a 16 bit dynamic range and therefore each pixel can have a value between -32 768 and 32 768, compared to a range which only stretches from 0 to 255, as is the case with an 8 bit chip. The result is that there is a lot more information contained in one image. This is illustrated in Figure 3.12 where the image depth of a single image is varied. The phosphor screen is imaged onto the camera by a 60 mm macro lens.

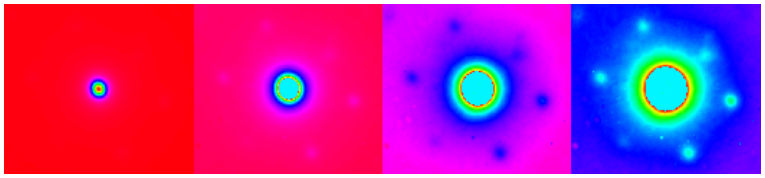

Figure 3.12: The information at different depths in a 16-bit image.

3.6 SAMPLE PREPARATION

The production of thin, freestanding specimens is one of the big challenges of electron diffraction in transmission geometry. Most materials cannot be examined by electron diffraction in their natural state because they are too thick. As already mentioned, the mean free paths of electrons are small due to the strong electron-matter interaction. Therefore samples need to be thin enough to allow the electrons to pass through and typically a thickness of less than 100 nm is required. In a standard Transmission Electron Microscope (TEM) the electron beam can be focused down to a diameter of less than 100 nm and a diffraction pattern can be obtained from a very small piece of sample. In UED experiments, the beam cannot be so tightly focused which means that, in addition to being very thin, samples which are laterally large (in the order of $100\,\mu\text{m} \times 100\,\mu\text{m}$) are needed to acquire a diffraction pattern.

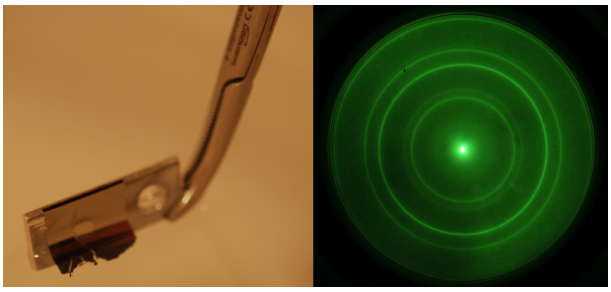

Figure 3.13: Picking up a gold foil after floating (left) and the diffraction pattern (right) obtained from a polycrystalline gold foil ($E_{electron} = 40\,keV$).

Various methods to produce thin films were proposed. Our first attempt was manufacturing gold and titanium films by depositing a thin layer of metal onto a microscope slide through electron

beam evaporation[2]. A water soluble substrate (for example a mix of betaine and sucrose) between the glass plate and the metal acts as a parting agent, enabling the floating of films on water and picking up of pieces onto a mesh. Samples with a diameter of up to 1 cm were created and a diffraction pattern from one of these gold foils is shown in Figure 3.13. This method works well, but it can only be used to produce polycrystalline samples and in order to investigate crystal structures, a different approach is needed.

The crystalline sample we prepared, $TiSe_2$, has a layered structure where each layer consists of three atomic sheets (Se–Ti–Se) which are bound together by strong covalent bonds. The different layers are only linked through weak van der Waals forces and due to this fact, we tried cleaving the sample using scotch tape. This seemed to work rather well at first, but as the samples got thinner they broke into very small pieces. Also it was not possible to dissolve the glue to separate the sample from the tape and glue contamination was inevitable. A variety of solvents (such as acetone, ethanol and tricholoroethylene) was tried without success.

The next step was to attempt cutting slices off a bulk crystal using a *Reichert Ultracut S* ultramicrotome[3]. *Ultramicrotomy* is the term used to produce sections of material thin enough for examination in the electron microscope [16]. It is an alternative to methods such as ion milling and electropolishing and has the benefit that the chemistry of the sample remains unchanged. The disadvantage is that the sample can be fractured or deformed, because the knife can either cut the sample or cause a partially controlled fracture [17]. The main challenge with cutting crystals like $TiSe_2$ is the alignment of the knife along the crystal plane. As already mentioned, $TiSe_2$ has a layered structure and the idea is to cut the crystal in such a way that the different layers are separated from each other, in the process minimising damage to the sample.

Biological samples and polymers are routinely cut by means of an ultramicrotome. These samples tend to be quite soft and have to be embedded in a hard resin[4] for support before slicing. With $TiSe_2$ samples we first glue a small piece ($\sim$1 mm $\times$ 1 mm) onto a resin block to ensure that the orientation of the crystal is more or less right. The top part of the block is then embedded in more resin to fix the position of the $TiSe_2$. To harden, the resin has to be baked at a temperature of 60°C for 24 hours.

In order to expose the sample, excess resin has to be cut away. This is done under a stereo microscope, using a razor blade to prepare a trapezoidal cutting face smaller than 1 mm$\times$1 mm. Next the sample block is mounted on the ultramicrotome arm (see Figure 3.14) and the knife is aligned with respect to it. There are two types of knives: glass and diamond. A glass knife is normally used to cut away the last resin and to make the surface flat. When that is done, it is replaced by a diamond knife which is much sharper and can be used to cut much harder materials (such as $TiSe_2$ crystals). Diamond knives come with a specified cutting angle (normally 4°) which reduces the pressure applied to the sample while cutting.

[2] With the help of Yvonne Kheswa, using the equipment at Ithemba Labs.

[3] Machine at the Electron Microscopy Unit, University of Cape Town. We were trained and assisted by Mohamed Jaffer.

[4] Resins are viscous liquids that can harden permanently. Commonly used in ultramicrotomy are epoxy resins which harden when baked at temperatures between 50°C and 120°C. There are also acrylic resins where hardening takes place when exposed to UV light. The sample embedded in the resin is referred to as the "specimen block".

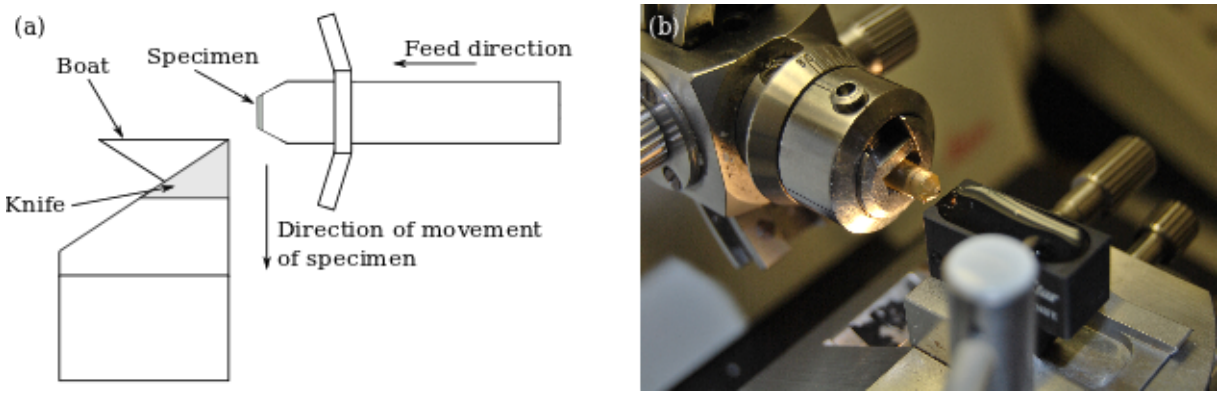

Figure 3.14: In (a) the basic principle of an ultramicrotome is demonstrated and (b) shows the *Reichert Ultracut S* ultramicrotome, the machine we used at UCT. The sample block, mounted on the ultramicrotome arm, the knife and the boat can be seen.

The principle (illustrated in Figure 3.14) on which an ultramicrotome operates is that an arm (carrying the sample) is moved past a sharp cutting edge (the knife) and the forces transmitted from the cutting edge to the specimen causes a thin section to detach from the face of the sample block [16]. Between cuts the arm is moved towards the knife in small steps (2.5 nm – 5 μm). Attached to the knife is a boat which contains a liquid (any appropriate medium, normally water) onto which the sections float and from where they are picked up onto a grid. It takes some time, patience and practise to learn this technique, but the result is samples which are thin and large enough to be used in our UED setup, as shown in Figure 3.15.

What is remarkable is that the mesh pictured in Figure 3.15 (c) is the one we used in the experiments discussed in Section 6. The sample gets 'pumped' (excited by the pump beam) 1 000 times per second (the laser has a repetition rate of 1 kHz) and recovers within 1 ms, before the next pulse arrives. To obtain one image, an exposure time of 60 s is required. A scan typically contains 80 images and a single measurement on average consists of 10 scans. This means that during a single scan a phase transition is initiated in the sample 5×10^7 times and that this specific 100 μm$\times$100 μm piece of $TiSe_2$ (which is indicated in Figure 3.15 (c) by the red square and is only 30 nm thick and) has undergone in the order of 10^9 phase transitions without any damage that we are aware of.

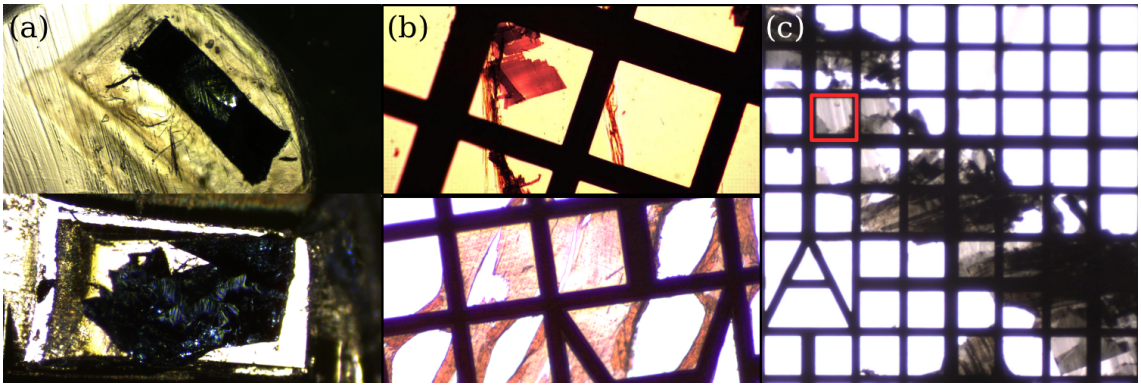

Figure 3.15: To cut thin samples, the surface of the sample block has to be prepared by cutting away excess resin. Panel (a) shows $TiSe_2$ inside a resin block (top) and a prepared trapezoidal cutting face (bottom). (b) shows samples on a grid after cutting with the *Reichert Ultracut S* ultramicrotome. The top sample is $TiSe_2$ and the bottom sample is Tetracene. In (c) the $TaSe_2$ used in the experiments discussed in Section 6 is shown on a grid where one square is $100\,\mu m \times 100\,\mu m$. The electron beam is focused onto the part of the sample indicated by the red square. This sample was prepared by Maximilian Eichberger.

3.7 RUNNING AN EXPERIMENT

The duration of a single experiment can be as long as 20 hours, but the execution is fully automated. After aligning the laser and electron beams, finding spatial overlap and determining time zero, the delay stage, camera, shutter (in the path of the pump beam) and beam correction are controlled by a computer. The necessary software for this was developed in *LabView* by PhD student Kerstin Haupt.

One exposure (typically over 60 s) is referred to as an image. Images are acquired at different time steps and one set of images at various delay times is called a scan. During a measurement a scan is typically repeated 10–15 times which means that for each time step there are 10–15 images (depending on the number of scans) containing information about the state of the sample at a certain time after excitation.

Before running a scan, the starting point on the delay stage and the ranges over which you want to scan, has to be set, as well as the number of scans you want to do. Many intervals, each with different step sizes and ranges, can be chosen. Next the calibration of the piezo mirrors for the pump and probe beam correction takes place and the initial coordinates (to which correction takes place) are logged. This calibration is repeated at the beginning of each new scan.

Each scan consists of an *unpumped* and *pumped* image at each time step. An *unpumped* image refers to a diffraction pattern where there is no laser pump pulse present and *pumped* is when the sample is excited by the laser. The unpumped image serves as a reference. This is controlled by an electronic shutter in

the path of the pump beam. After both images are acquired for a certain delay time, the stage is moved to the next position, beam correction takes place and new images are obtained. The time, stage position, whether the shutter is open or closed and the coordinates of the pump and probe beams (before and after acquiring images) are all stored in a log file.

Another thing to consider when running an experiment is the temperature of the sample. To monitor this we use *Pt-100* temperature sensor mounted on the sample holder. The magnetic lens heats up and when the chamber is not in thermal equilibrium we see a drift of the translation stages which means that we lose the diffraction pattern. The sample is thermally isolated from the base plate, but some heat does go through. However, we found that the sample never gets warmer than 28°C, even though the base plate reaches temperatures as high as 36°C.

The fluence of the pump beam is controlled by a $\lambda/2$- wave plate and polariser in the pump path before it enters the vacuum chamber and the pulse energy is measured by a *Thorlabs S120VC* photo diode sensor head with a *PM100A* USB interface.

The samples are mounted a distance of approximately 2 cm behind the magnetic lens and a voltage of 20 V is applied to the sample holder to capture photo electrons and to prevent the sample holder from being charged up. We found that applying this voltage significantly reduced the background by capturing the photo electrons, which are due to the strong pump pulse.

With all the improvements discussed in this section in place and the characterisation of the system complete, the next step was to do experiments on a suitable and interesting sample to prove that the setup works.

Part II

ULTRAFAST ELECTRON DIFFRACTION ON THE TRANSITION-METAL DICHALCOGENIDE $4H_b$-$TaSe_2$

In the next part of this thesis I will describe the first time-resolved measurements that were done with our UED setup. In Section 4 I will describe the properties and characteristics of the sample we used in the experiment, $4H_b$-$TaSe_2$. A short explanation of electron diffraction will be given in Section 5 to demonstrate why electron diffraction patterns are formed and what we can learn from them, followed by a discussion of the results that were obtained for the sample $4H_b$-$TaSe_2$ in Section 6.

4 THE TRANSITION-METAL DICHALCOGENIDE $4H_b$ -$TaSe_2$

Layered transition-metal dichalcogenides (TMD) are denoted by the general formula MX_2, where M refers to a transition-metal (Ti, Ta, Se, etc.) and X to a chalcogen atom (O, S, Se, Te). Each layer consists of three atom-thick sheets (a transition-metal sheet interposed between two chalcogen sheets) which are bound together by strong covalent bonds. The layers are stacked on top of each other (along an axis perpendicular to the sheets) and linked through weak van der Waals interactions. The chalcogen atoms are hexagonally packed and the transition-metals can have either octahedral or trigonal prismatic coordination. The stacking can take place in various sequences - simply octahedral or trigonal prismatic layers, or some combination of the two - and this leads to polytypism. To distinguish between different TMD polytypes, a prefix is added to the chemical formula (MX_2). The prefix consists of a number which corresponds to half of the number of chalcogen sheets per unit cell and a letter which indicates the symmetry of the unit cell – T=trigonal, H=hexagonal and R=rhombohedral. For polytypes with an equal number of chalcogen sheets and identical unit cell symmetry, a letter (a, b, c) is added as a subscript. 1T-polytypes consist of layers with solely octahedral coordination and 2H-polytypes are made up of trigonal prismatic layers. The rest are all a mixture of the two. [18, 19, 20]

In many transition-metal dichalcogenides there spontaneously occurs a modulation of the electron density when the material is below a certain critical temperature and the modulation of the electron density is called a charge density wave (CDW) [21]. This modulation of the electron density goes hand in hand with a periodic lattice distortion (PLD) of the atomic positions. This is illustrated for a 1D-crystal in Figure 4.1. The CDW is said to be either commensurate or incommensurate, where commensurate

refers to a CDW with a wavelength which is a multiple or a rational fraction of the lattice constant. It this is not the case, the CDW is incommensurate.

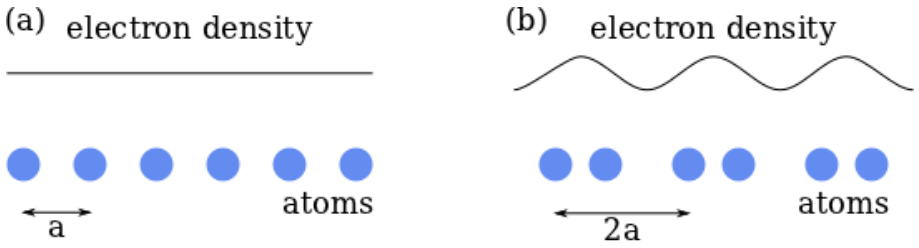

Figure 4.1: (a) shows a crystal with a lattice constant a and a uniform electron density and in (b) the lattice and electron density are periodically modulated. A periodically modulated electron density is called a charge density wave (CDW).

The TMD we used in our study is $TaSe_2$ and there are six different polytypes: 1T-$TaSe_2$, 2H-$TaSe_2$, 3R-$TaSe_2$, $4H_a$-$TaSe_2$, $4H_b$-$TaSe_2$ and 6R-$TaSe_2$ [20]. The polytype we investigated is $4H_b$-$TaSe_2$ and we chose it for a few simple reasons. Firstly, one of the most technical and comprehensive studies in UED has recently been done on a similar sample (1T-TaS_2) [8]. Doing an experiment on $4H_b$-$TaSe_2$ was a good way for us to bring our system up to state of the art level and to establish that we are indeed capable of carrying out a successful experiment. The second reason is that we met Maximilian Eichberger who was involved in the experiment on 1T-TaS_2 and were supplied with $4H_b$-$TaSe_2$ samples. The fact that the experiment can be done at room temperature made it the ideal sample for our setup.

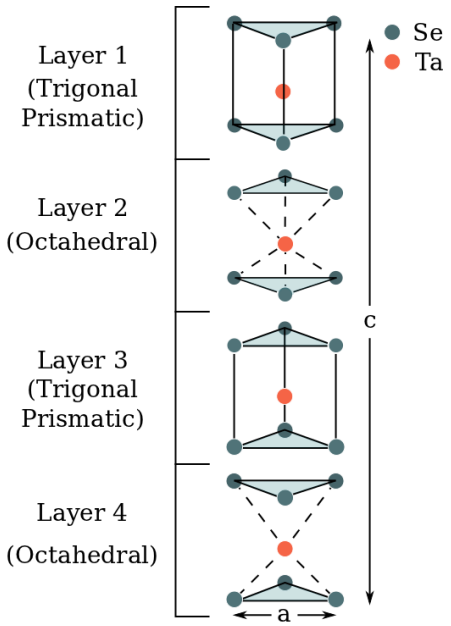

Figure 4.2: The unit cell of $4H_b$-$TaSe_2$.

$4H_b$-$TaSe_2$ has alternating octahedral and trigonal prismatic layers. The unit cell of $4H_b$-$TaSe_2$ (in the metallic phase where T>600 K) is shown in Figure 4.2. Two CDWs develop at well defined temperatures. In the octahedral layers an incommensurate CDW forms at 600 K and it locks into a commensurate $(\sqrt{13}a_0 \times \sqrt{13}a_0 \times c_0)$ superstructure at 410 K, where in the trigonal prismatic layers an incommensurate CDW forms below 75 K [22]. Initially it was thought that the modulation at room temperature only takes place within the octahedral layers, but later it was established that there are significant modulation amplitudes in the trigonal prismatic layers, about 1/10 of that in the octahedral layers [23]. The space group of the normal metallic phase (>600 K) is $P6_3/mmc$ and the lattice parameters are $a_0 = b_0 = 3.46$ Å and $c_0 = 25.15$ Å

[24]. The formation of the CDW results in a periodic lattice distortion where 13 Ta atoms cluster together. The central Ta atom remains in the same position while its 12 nearest neighbours move closer to it. This displacement takes place in the a-b plane and there is almost no change along the c-axis. The modulation is illustrated in Figure 4.3 where the Ta plane in the metallic phase and a modulated Ta plane are shown. A summary of the properties of $4H_b$-$TaSe_2$ is given in Table 4.1.

Table 4.1: The different temperature-dependent phases of $4H_b$-$TaSe_2$. The modulation wave vectors are given in reciprocal space.

Temperature (K)	Phase	Layers Involved	Modulation Wave Vector
>600	Normal metallic		
410 - 600	Incommensurate	Octahedral	$\mathbf{q}^{\mathrm{T}} = 0.265\mathbf{a_0^*}$
75 - 410	Commensurate	Octahedral	$q^T = \frac{1}{\sqrt{13}}a_0^*;\alpha,\beta$ superlattices
<75	Incommensurate	Trigonal Prismatic	$\mathbf{q}^{\mathrm{H}} = \mathbf{a_0^*}/3(1+\delta)$, at 10 K, $\delta = 0.04$
	Commensurate	Octahedral	$q^T = \frac{1}{\sqrt{13}}a_0^*;\alpha,\beta$ superlattices

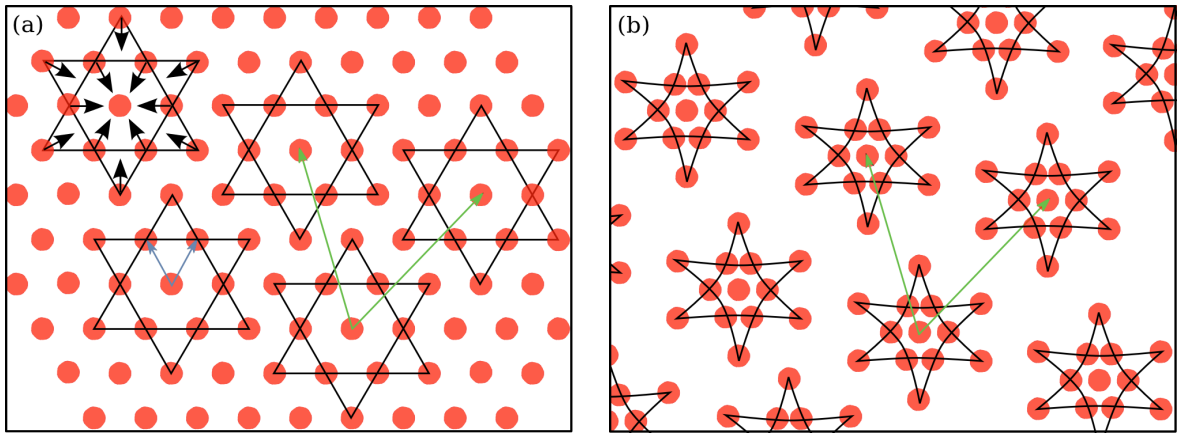

Figure 4.3: The modulation of the crystal lattice of $4H_b$-$TaSe_2$ in the Ta-plane when it goes from the metallic to commensurate CDW phase. (a) shows the Ta plane of $4H_b$-$TaSe_2$ in the metallic phase. The black arrows indicate the direction of the movement of the atoms (the size is not relative) when it goes from the metallic to commensurate CDW phase. The blue arrows indicate the lattice vector of $4H_b$-$TaSe_2$ in the metallic phase (T>600 K) and the green arrows when it is in the commensurate CDW phase (75 K < T < 410 K). In the commensurate CDW the 12 nearest Ta atoms approaches the central Ta atom. This is shown (but not in a relative way) in (b).

5 ELECTRON DIFFRACTION

Since the discovery of electron diffraction in 1927 by Clinton Davisson and Lester Germer [2] it has been used as a powerful tool to determine the structure of crystalline materials. The spatial resolution of a transmission electron microscope (TEM) is good enough to determine the arrangement of individual atoms and even defects, such as dislocations and stacking faults, can be observed.

In this Section I will describe the basic theory of electron diffraction – how the interaction of electrons with matter leads to the formation of a diffraction pattern, followed by the information that can be extracted from it. The analysis of an electron diffraction pattern is illustrated by a practical example based on the specimen described in Section 4 ($4H_b$-$TaSe_2$) which is the sample used in the experiment discussed in Section 6.

5.1 THE FORMATION OF AN ELECTRON DIFFRACTION PATTERN

Electrons are negatively charged particles. They also exhibit wave properties manifested through their de Broglie wavelength, $\lambda_{dB} = {}^{h}/_{p}$. Due to their negative charge, the particles are deflected through Coulomb interactions by shell electrons or the nucleus when passing close to an atom and this leads to scattering. On the other hand, electron diffraction (which is a wave characteristic) occurs because of the interaction between different electron waves. According to Williams and Carter [17], the term scattering might best apply to particles and diffraction to waves, which means that both are valid for electrons and that diffraction is a special form of elastic scattering which is utilised in transmission electron microscopy.

Electrons interact strongly with matter and this can result in the formation of a diffraction pattern from which structural information about the matter can be obtained. Single crystals will lead to the formation of diffraction patterns which contain regularly spaced, discrete spots, while polycrystalline samples (composed of many randomly orientated small single crystals) give patterns with concentric rings, see Figure 5.1 (a) for examples. Incoming electrons can also knock out inner shell electrons by transferring energy to an individual atom and this means that when matter is bombarded by electrons, a variety of secondary signals can be generated. As indicated in Figure 5.1 (b), electrons can either pass through the sample without interaction, be scattered backwards or be elastically or inelastically scattered in a forward direction. Additionally, X-rays (characteristic lines and Bremsstrahlung), visible light and secondary and Auger electrons can be produced. Many of these processes mainly depend on the energy of the incoming electrons and the size (or charge) of the nuclei. In transmission electron microscopy the (inelastically and elastically) forward scattered electrons, as well as the direct beam, are detected.

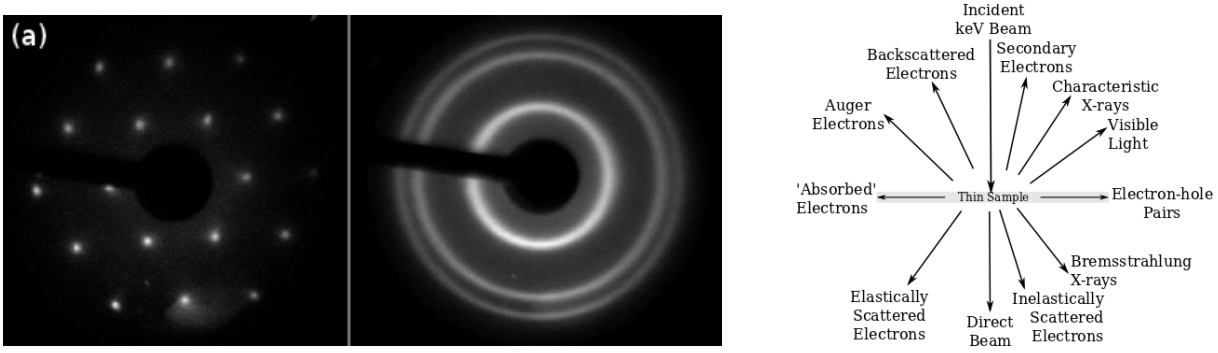

Figure 5.1: When electrons interact with matter, diffraction patterns can be formed by elastically scattered electrons. (a) shows a diffraction pattern from crystalline graphite on the left and polycrystalline graphite on the right. In (b) the different signals which are generated during electron-matter interaction are illustrated. The direction shown for each signal does not always represent the physical direction, but indicate (in a relative manner) where the signal is strongest and usually detected [17].

The wave-particle duality of electrons (or more specifically particles with a rest mass of $m_0 \neq 0$) was first suggested by Louis de Broglie in 1924 [25], who related the wavelength (λ) of particles to their momentum (and therefore energy) by the De Broglie relation:

$$\lambda = \frac{h}{p}. \tag{5.1}$$

Making use of the relativistic energy-momentum relation ($E^2 = p^2c^2 + m^2c^4$) and the fact that $E = E_{kin} + E_0$, the de Broglie wavelength for electrons can be calculated by

$$\lambda_e = \frac{hc}{\sqrt{E_{kin}(2E_0 + E_{kin})}} \tag{5.2}$$

where E_{kin} is the kinetic energy of the electron (after acceleration due to the high voltage), E_0 is the rest energy of the electron and h is Planck's constant and c the speed of light, all as defined in Table 5.1. When applying an acceleration voltage of 30 keV, the corresponding electron wavelength is 6.98 pm = 0.0698 Å. This is important, because in order for diffraction to take place the wavelength of the incoming electrons should be smaller than the atomic lattice spacing, which is typically in the order of 1 Å, e.g. 3.46 Å in our $TaSe_2$ sample. It is also much shorter than the

Table 5.1: Important constants and definitions

h (Planck's constant)	6.62×10^{-34} J s
m_e (rest mass of electron)	9.11×10^{-31} kg
c (speed of light)	3×10^{8} m/s
e (charge of an electron)	1.602×10^{-19} C
1 eV	1.602×10^{-19} J
E_0 (rest energy of electron)	m_ec^2=511 keV
E_{kin} (after acceleration)	e×voltage

wavelength of visible light (400 – 700 nm), which means that electrons can be used to image materials with a much better resolution than a normal optical microscope.

To understand why we see an electron diffraction pattern, we look at Bragg's Law[5]:

$$2d\,sin\,(\theta) = n\lambda \tag{5.3}$$

which gives a reciprocal relationship between θ (the angle between the incoming electron beam and the diffracting plane of atoms) and d (the interplanar distance) as illustrated in Figure 5.2 (a). λ is the wavelength of the incident electrons and from wave theory we know that constructive interference takes place when waves are in phase and that diffracted waves are in phase when the path difference is $n\lambda$; $n\epsilon N$. This means that only when Bragg's Law is satisfied, will an incoming wave be diffracted from a specific lattice plane (hkl) (this notation is explained in Section 5.2) in such a way that the diffracted waves interact constructively to form a diffraction pattern. When the incoming electron beam falls onto the crystal planes at an angle where the requirements of Bragg's Law are not met, destructive interference occurs and no diffraction pattern can be observed. When constructive interference occurs, the wave vectors of the incoming and diffracted waves (respectively labeled $\mathbf{k}_\mathrm{i}$ and $\mathbf{k}_\mathrm{d}$) are related by the scattering angle θ and in reciprocal space the scattering vector $\mathbf{K}$ can be defined as

$$\mathbf{K} = \mathbf{k}_i - \mathbf{k}_d \tag{5.4}$$

where $\mathbf{K}$ represents the change in the wave vectors of the plane wave and $|\mathbf{K}| = \frac{4\pi}{\lambda} sin\theta$ (refer to Figure 5.2(b) to see this from the geometry). Also notice that it is assumed that the scattering is elastic and therefore $|\mathbf{k}_i| = |\mathbf{k}_d|$ and because this is in reciprocal space, the vectors have reciprocal length units [m^{-1}]. The reciprocal lattice vector is defined as $\mathbf{g}$ and the von Laue condition stipulates that

$$\mathbf{K} = \mathbf{k}_i - \mathbf{k}_d = \mathbf{g} \tag{5.5}$$

which is easily shown to be equivalent to Bragg's Law.

[5] Bragg's Law describes diffraction based on reflection and the term "Bragg reflection" is commonly used to describe diffraction in transmission electron microscopy.

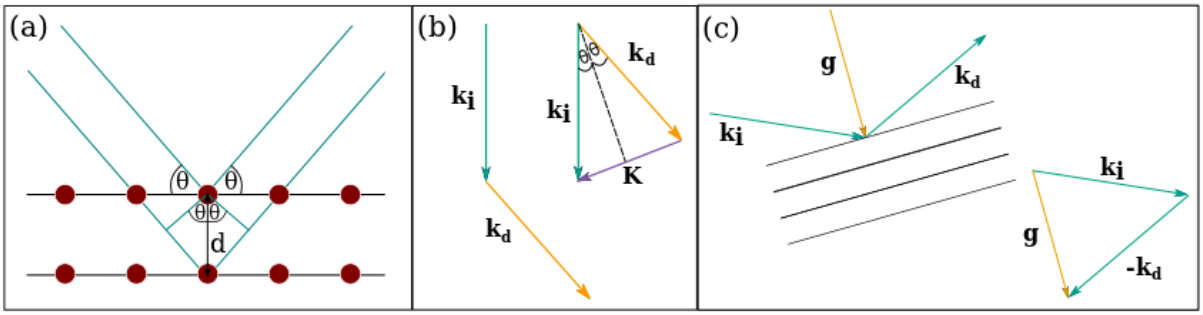

Figure 5.2: Panel (a) illustrates Bragg's Law ($2d\,sin\,(\theta) = n\lambda$) which states that if waves (with a wavelength λ) are reflected from parallel planes (which are spaced a distance d apart) and the angle of the incident and reflected waves with respect to the parallel planes is θ, the total path difference between the waves reflected from the parallel planes is $2d\,sin\,(\theta)$. In panel (b) the relationship between the incoming ($\mathbf{k}_\mathrm{i}$), diffracted ($\mathbf{k}_\mathrm{d}$) and scattering ($\mathbf{K}$) wave vectors is given and in (c) the reciprocal lattice vector $\mathbf{g}$ is shown. Bragg's Law is satisfied when $\mathbf{g} = \mathbf{k}_i - \mathbf{k}_d = \mathbf{K}$.

5.2 THE INFORMATION OBTAINED FROM AN ELECTRON DIFFRACTION PATTERN

Diffraction patterns contain two basic types of information[6]:

1. Spatial arrangement – the distances (R) between the central and other diffraction spots or rings and the angles (ϕ) between the lines that join the central spot to each diffraction spot

2. Intensity of diffraction spots.

From this one can determine elements such as whether the sample is crystalline or polycrystalline, the lattice parameters and crystal lattice, as well as the composition of the material. However, before that can be done a few things need to be understood.

A crystal is a solid object where a basic pattern of atoms is repeated over and over in all three dimensions and the smallest repeating volume of the lattice is called the unit cell [27]. Each unit cell is characterized by the lattice spacings (a, b, c) along three major axes (x, y, z) and the angles (α, β, γ) between these major axes. By definition α is the angle between the y and z axes, β between the x and z axes and γ between the x and y axes. Specific combinations of these parameters (a, b, c and α, β, γ) give rise to different crystal systems. In total there are seven crystal systems, as listed in Table 5.2. There can exist variations of each crystal system and these are referred to as crystal lattices. For example, a cubic crystal system may have an atom at the centre of the unit cell and is known as a Body-Centered Cubic unit cell. There are fourteen crystal lattices, as shown in Table 5.2, with P = Primitive, I = Body-Centered, F = Face-Centered, C = One Face-Centered.

[6]The primary source used in this section is the book by Beeston, Horne and Markham [26].

Table 5.2: The seven crystal systems and their corresponding lattice parameters and possible crystal lattices (also called Bravais lattices). An illustration of these lattices can be found in Appendix 1 in Reference [26].

Crystal System	Lattice Spacings	Angles Between Axes	Crystal lattices
Cubic	$a = b = c$	$\alpha = \beta = \gamma = 90°$	P, I, F
Tetragonal	$a = b \neq c$	$\alpha = \beta = \gamma = 90°$	P, I
Orthorhombic	$a \neq b \neq c$	$\alpha = \beta = \gamma = 90°$	P, I, F, C
Rhombohedral (Trigonal)	$a = b = c$	$\alpha = \beta = \gamma < 120° \neq 90°$	P (R)
Hexagonal	$a = b \neq c$	$\alpha = \beta = 90°; \gamma = 120°$	C
Monoclinic	$a \neq b \neq c$	$\alpha = \gamma = 90° \neq \beta$	P, C
Triclinic	$a \neq b \neq c$	$\alpha \neq \beta \neq \gamma \neq 90°$	P

The information in an electron diffraction pattern can be used to determine the spacing between the lattice planes (referred to as d-spacings) which give rise to the particular spot by applying the basic formula

$$d = \frac{\lambda L}{R} \tag{5.6}$$

to each diffraction spot, where R is the distance between the centre spot (direct beam) and the Bragg reflection, L is the distance from the sample to the camera and λ is the wavelength of the electrons. The formula is derived from Bragg's Law ($\lambda = 2d\,sin\theta$) and the basic geometry of an electron microscope where $tan2\theta = R/L$ (see Figure 5.3).

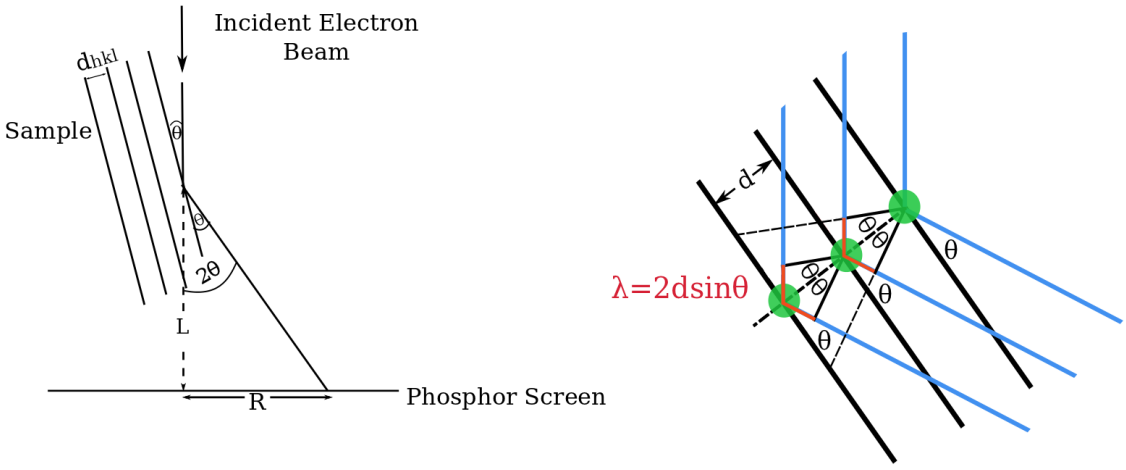

Figure 5.3: The basic geometry of an electron diffraction camera. Combining this geometry with Bragg's Law and the approximation that θ is small (and therefore that $tan2\theta = 2sin\theta$) Equation 5.6 can be derived.

Lattice planes are labeled by the allocation of Miller indices, a universally approved system where the indices h, k and l are defined as the reciprocals of the intercepts that any particular plane makes along the three major axes, in terms of the lattice parameters a, b and c [26]. This means we can define the Miller indices as

$$(h\,k\,l) = \left(\frac{a}{x_{intercept}} \; \frac{b}{y_{intercept}} \; \frac{c}{z_{intercept}} \right). \tag{5.7}$$

Planes which are crystallographically equivalent are represented by {h k l} and the direct beam is always labelled (0 0 0). Refer to Figure 5.4 for the illustration of a simple cubic unit cell and its lattice parameters and lattice planes, as well as some of the possible lattice planes in a two-dimensional hexagonal structure.

In the diffraction pattern, each diffraction spot or ring has to be assigned the Miller index of the lattice plane from which it arises. When the structure of a specimen is known, the relationship between the lattice spacing (d, calculated by using Equation 5.6), the lattice parameters (a, b, c), the angles between the major axes (α, β, γ) and the Miller indices (h, k, l) can be established by selecting the appropriate formula for the crystal system of the sample from Appendix 2a in Reference [26]. The standard procedure is to insert the values for d, a, b and c (and α, β, γ if the formula for the crystal system requires it) and then determine the values of h, k and l for each diffraction spot. I will demonstrate the indexing of the diffraction pattern of $4H_b$ -$TaSe_2$ which is the sample used in the experiments discussed in Section 6. More information on the specimen is given in Section 4.

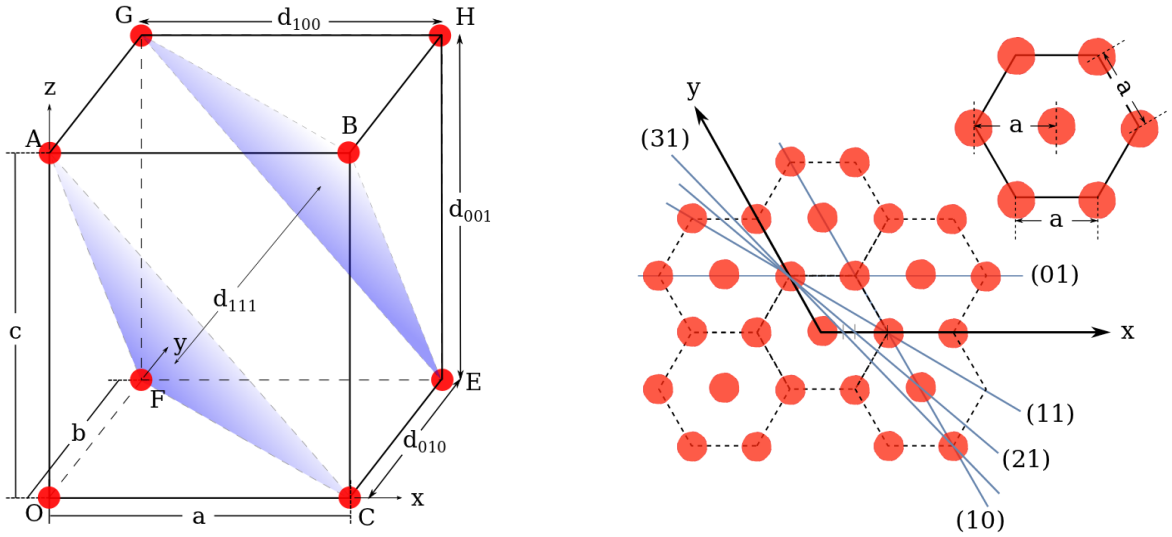

Figure 5.4: On the left is an illustration of a simple cubic unit cell showing the lattice parameters, some lattice planes and the d-spacings between the planes. On the right some of the possible lattice planes in a two-dimensional hexagonal structure is shown. The sample we investigated ($4H_b$ -$TaSe_2$) has a hexagonal structure.

$4H_b$ -$TaSe_2$ is part of the family of transition-metal dichalcogenides which all belong to the hexagonal crystal system and the appropriate d-spacing formula for hexagonal crystal systems is given by

$$\frac{1}{d^2} = \frac{4}{3}\left(\frac{h^2 + hk + k^2}{a^2}\right) + \frac{l^2}{c^2}. \tag{5.8}$$

If we define P = h^2 + hk + k^2, where h and k are the Miller indices, P can have the values 1, 3, 4, 7, 9, ... and from Equation 5.6 we see that $R^2 \sim \frac{1}{d^2}$. The average of the measured R-distances (as indicated in Figure 5.5) are listed in Table 5.3 and by comparing the ratios of ${R_n}^2$ ($\frac{1}{d_n^2}$) and ${R_1}^2$ ($\frac{1}{d_1^2}$), we see a pattern of 1, 3, 4, 7, 9, ... From this we can conclude that all the reflections in this diffraction pattern are {h k 0} reflections which means that we can only determine the lattice parameter a from this diffraction pattern (by using Equation 5.8). If the Miller index l = 0, all the lattice planes that give rise to diffraction spots are parallel to the z axis (they do not intersect the z axis) and we can say that the electron beam is travelling along the z axis. To observe diffraction patterns where l $\neq$ 0 in order to obtain information about the lattice parameter c, the sample has to be tilted with respect to the incoming electron beam. However, the charge density wave that we want to observe only occurs because of a modulation of the lattice parameter a along the x and y axes and therefore this orientation is sufficient for our purposes. See Figure 4.2 for the unit cell of $4H_b$ -$TaSe_2$.

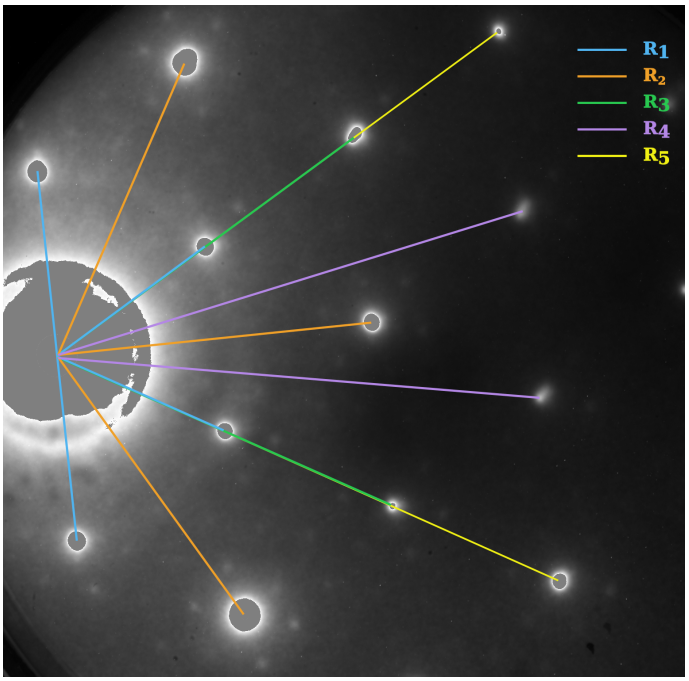

Figure 5.5: The diffraction pattern of $4H_b$-$TaSe_2$. The measured distances (R_n) between the centre spot and different diffraction spots are listed in Table 5.3.

Table 5.3: The values of R (as measured on the diffraction pattern), d (as calculated using Equation 5.6 with the values L = 300 mm and λ= 7.67 $\times 10^{-12}$ m for the corresponding electron energy of 30 keV) and the lattice parameter a (from Equation 5.8). From the ratios between $d_n{}^2$ and $d_1{}^2$ we can see that the Miller index l = 0.

n	R_n (mm)	d (m)	$\frac{R_n^2}{R_1^2} = \frac{d_1^2}{d_n^2}$	P=h^2+hk+k^2	Possible values of (hkl)	a (Å)
1	7.7	2.99×10^{-10}	1	1	(100), (010), (1$\bar{1}$0)	3.45
2	13.2	1.74×10^{-10}	2.9	3	(2$\bar{1}$0), (110), (1$\bar{2}$0)	3.48
3	15.3	1.50×10^{-10}	3.9	4	(200), (020), (2$\bar{2}$0)	3.46
4	20.1	1.14×10^{-10}	6.8	7	(3$\bar{1}$0), (210), (3$\bar{2}$0)	3.48
5	22.7	1.01×10^{-10}	8.7	9	(300), (030), (3$\bar{3}$0)	3.50

To index a diffraction pattern, we just need to know the Miller indices of two of the diffraction spots right next to the centre spot and from that the rest of the spots can be labeled by making use of vector addition. Negative values are indicated by a bar above the number. The diffraction spots which are a distance R_1 from the centre spot has to satisfy P = h^2 + hk + k^2 = 1. This means (h k l) must be (1 0 0) or (0 1 0). The index (1 0 0) can be arbitrarily assigned to any spot a distance R_1 from the central spot. The angle between the two lines that join two diffraction spots to the direct beam should be as specified by the appropriate interplanar angle formula given in Appendix 2b in Reference [26]. For hexagonal crystal systems the interplanar angle formula is

$$cos\phi = \frac{h_1h_2 + k_1k_2 + \left(\frac{h_1k_2+k_1h_2}{2}\right) + \frac{3a^2}{4c^2}l_1l_2}{\sqrt{\left(h_1^2 + k_1^2 + h_1k_1 + \frac{3a^2}{4c^2}l_1^2\right)\left(h_2^2 + k_2^2 + h_2k_2 + \frac{3a^2}{4c^2}l_2^2\right)}}. \tag{5.9}$$

where ϕ is the angle between the spots labeled (h_1 k_1 l_1) and (h_2 k_2 l_2) on the diffraction pattern. This means that for (1 0 0) and (0 1 0), $cos\phi = \frac{1}{2}$ which corresponds to an angle of $\phi = 60^\circ$. Therefore the angle between (1 0 0) and (0 1 0) must be 60° and from these two labels the rest of the diffraction pattern can be indexed. The diffraction pattern of $4H_b$ -$TiSe_2$ and its Miller indices are shown in Figure 5.6. To be complete and as a measure to check if the indices were assigned correctly, the interplanar angle can be calculated for a number of spots on the diffraction pattern. Common reciprocal lattice selections (Miller indexing) for known crystal systems are given in Appendix 4 in Reference [26]. Hexagonal crystal systems are often labeled by (h k i l) where i = − (h + k). The extra index does make certain symmetries more obvious, but it is actually a redundant label.

Going back to equation 5.8, it is now possible to calculate the lattice parameter a (listed in Table 5.3 for the different d-spacings) and the average of a = 3.47 Å corresponds well to the known value of the lattice parameter which is a = 3.46 Å.

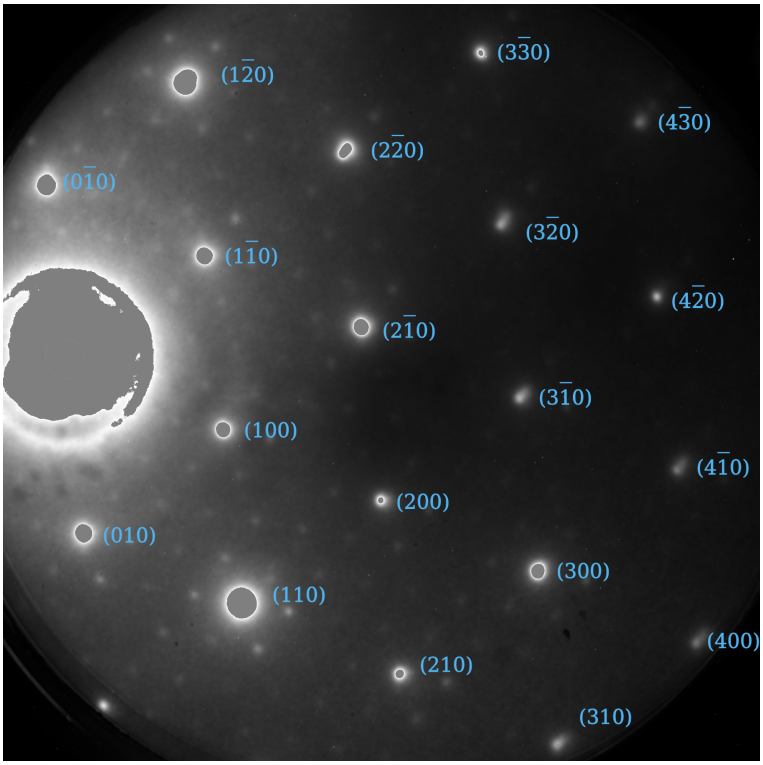

Figure 5.6: The diffraction pattern of $4H_b$-$TaSe_2$ in the commensurate CDW phase with the Miller Indices assigned to each Bragg reflection. The hexagonal superstructure around each Bragg reflection is due to the PLD which accompanies the formation of the CDW.

When carefully observing Figure 5.6, we see that the diffraction spots to which Miller Indices are assigned are not the only diffraction spots in the image. Around each Bragg reflection there is a visible hexagonal structure which is called a superstructure. This superstructure appears when the crystal is in the commensurate charge density wave phase (as explained in Section 4) and the dynamics of the periodic lattice distortion associated with this commensurate ($\sqrt{13}a_0 \times \sqrt{13}a_0 \times c_0$) CDW which occurs at temperatures between 75 K and 410 K is what we want to investigate. The signal of the superstructure is much weaker than that of the lattice, because only one electron per Ta atom contributes to the CDW and therefore its diffraction pattern.

Electron diffraction enables us to directly probe the structure of the crystal and a change in the intensity of the rings or spots in a diffraction pattern indicates a breakup of the lattice planes. This is what we want to investigate – how the structure changes when we deposit energy into the system. In order to do that, we had to develop a method to carefully extract information from the diffraction images we acquire. As already mentioned, a diffraction pattern is obtained with a 1 minute exposure, thereby integrating over 60 000 electron pulses, and this is referred to as an image. At each position of the delay

stage pumped and unpumped images are acquired and the collection of images at different time steps is called a scan. A typical measurement consists of 10 scans which means that in the end 10 images are obtained for different times after photoexcitation. Each pixel in the 16-bit image (the size of the chip is 2 048×2 048) can have a value between -32 768 and +32 768 and this information is converted to a 2D-array. The reason for this is to ensure that no information is lost during the averaging process. 32 768 is added to each element so that the value of each array entry lies between 0 and 65 536. Next we sum over all the arrays at a certain time position, divide by the number of scans and then the array is converted back to an image which is referred to as an average image. In Figure 5.7 the difference between a Bragg reflection of a single image and the Bragg reflection of an averaged image (10 scans) is shown and it is obvious that the signal to background ratio has improved.

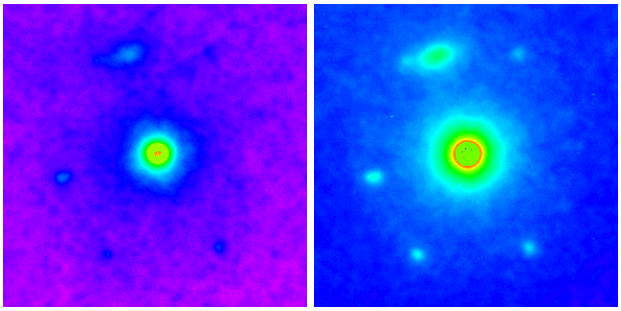

Figure 5.7: The Bragg reflection of a single image is shown on the left and on the right is the same reflection averaged over 10 images. In the averaged image the CDW superstructure is clearly visible.

The next step in analysing the data is to identify the Bragg reflections. This is done by setting an adjustable threshold where pixels with a value below it are set to 0 and pixels above it to 255. The output image is only 8-bit (Figure 5.8 (a)) and Bragg peaks are selected according to their size by defining minimum and maximum radii. The 16-bit image can also be viewed (Figure 5.8 (b)) and unwanted spots can be deselected. After this, a mask (see Figure 5.8 (c)) is fitted to each Bragg reflection and its corresponding CDW reflections. The final step is to evaluate the mask applied to each individual Bragg reflection and its accompanying CDW reflections. In Figure 5.8 (d) the green circles are for CDW peaks and the red circles indicate where the inelastic background scattering is evaluated. This has to be done because all Bragg reflections of the lattice, as well as the reflections from the CDW, sit on a background plane which is not necessarily planar.

For each averaged image an average integrated intensity over all the selected Bragg reflections is obtained and similarly an integrated average intensity over all the CDW superstructure reflections. The integration takes place over the area specified by the mask, see Figure 5.8 (c) for an example of such a mask. In the end the result is integrated values for the Bragg and CDW reflections of each averaged image. Finally we want to determine the difference in intensity between the unpumped intensity ($I(t<0)$) and the pumped intensity (I) with respect to time. To do this the relative change in intensity ($\frac{\Delta I}{I_0} = \frac{I-I_0}{I_0}$) at each time step is plotted to give a transient CDW signal and a transient Bragg signal which respectively tracks the change in the intensity of the CDW and Bragg reflections.

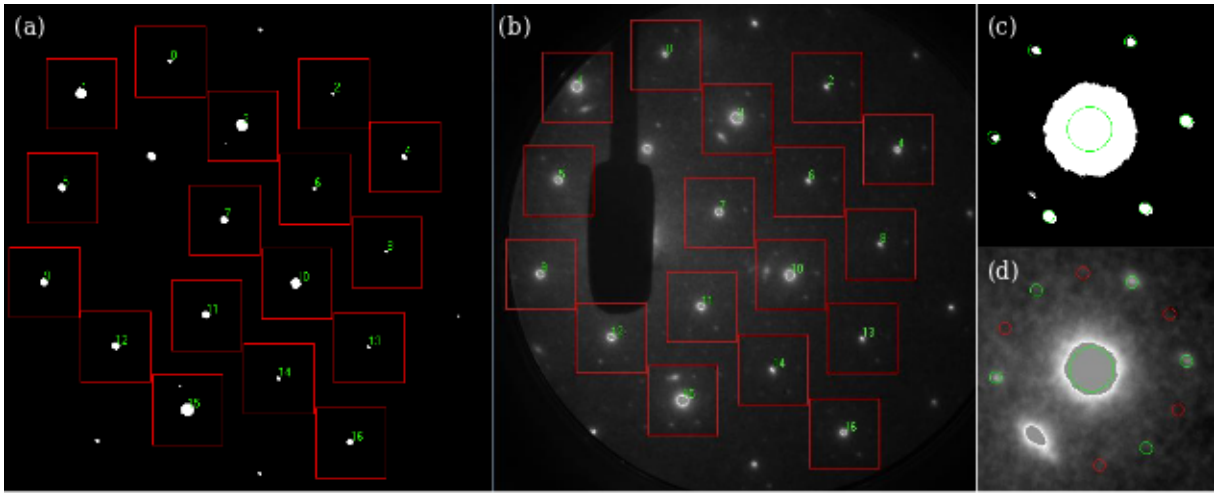

Figure 5.8: The procedure to analyse diffraction data. In (a) the desired Bragg reflections are selected. It is possible to view the 16-bit image (b) to ensure that no undesired spots are picked. (c) shows the mask which is fitted to a Bragg peak and its corresponding CDW reflections. Shown in (d) is the Bragg mask and CDW mask applied to each reflection to obtain an integrated value. The small green circles are for CDW reflections and the red circles are where the background is evaluated. The circles can be deselected if necessary, as was done in this case. The shadow which can be seen in (b) is a beam block which is moved into the direct electron beam to preserve the phosphor screen.

6 RESULTS: ULTRAFAST ELECTRON DIFFRACTION EXPERIMENTS ON $4H_b$ -$TaSe_2$

The transition-metal dichaclogenide $4H_b$-$TaSe_2$ is a charge density wave (CDW) compound which has a commensurate CDW phase when 75 K < T < 410 K. In the range 410 K<T<600 K it is in an incommensurate CDW state, while at T>600 K it occupies the metallic state. The development of a CDW, which is a periodic modulation of the electron density, is accompanied by a periodic lattice distortion (PLD) which is what we are capable of investigating by making use of electron diffraction. For more information on the sample, see Section 4.

The various structures of the crystal in its respective phases are well known, as are the temperatures at which the phase transitions occur. Extensive studies on the static structure of $4H_b$-$TaSe_2$ in its various phases have been done, utilising X-ray diffraction [22, 23] and electron and neutron diffraction [28] techniques. Time-resolved diffraction experiments, studying the atomic motion of the PLD, have been performed on other transition-metal dichalcogenides, such as 1T-TaS_2 [8] and 1T-$TiSe_2$ [29]. However, to date, no investigation of the dynamics of the atomic motion associated with the PLD which takes place when $4H_b$-$TaSe_2$ transitions from one phase to another, has been done. Making use of ultrafast electron diffraction (UED) we were, for the first time, able to study the structural dynamics of $4H_b$-$TaSe_2$ on sub-picosecond time scales.

At room temperature $4H_b$-$TaSe_2$ is in the commensurate CDW phase and in the electron diffraction pattern a hexagonal superstructure, due to the PLD, is visible around each Bragg reflection (see Section 5.2 for more information and an example of such an electron diffraction pattern). The photoexcitation of the sample at room temperature perturbs the CDW and this initiates a change in the structure and the intensity of the superstructure reflections (I_{CDW}). We monitor this in order to obtain information on the temporal evolution of the structural order of the PLD. The suppression of the CDW depends on the amount of energy which is deposited into the system and if enough energy is put into the system, comparable to the amount of energy needed to heat the sample to the incommensurate CDW phase, the CDW is destroyed completely and the phase transition to the incommensurable phase might have been induced. There is also an accompanying change in the intensity of the Bragg peak (I_{Bragg}) with a slight increase of scattering into the Bragg reflections. Our aim was to directly investigate the structural dynamics of the PLD by applying our laser pump electron probe technique. Whether the phase transition is induced might be determined from the signature of the CDW in the diffraction pattern and the time constant of its recovery.

The procedure of running an experiment is described in Section 3.7. All results discussed below were obtained from ultrafast electron diffraction experiments done on a single crystalline $4H_b$-$TaSe_2$ sample with a thickness of 30 nm. The properties of the electron probe beam are described in Section 3.2. Experiments were done with 30 keV electron bunches. A UV pulse energy of 110 pJ was used to produce the electrons and this results in 1 000 electrons per pulse and a pulse duration of 200 fs at the sample.

The pump pulse, with $\lambda = 775\,\text{nm}$, $h\nu$ =1.5 eV and τ =150 fs, is responsible for the photoexcitation and incidents on the sample at a slight angle. The pump beam diameter on the target is 600 μm, as has been measured by the pump beam correction camera, see also Section 3.4. The pulse energy can be adjusted by a $\lambda/2$-plate and polarizer. To determine the fluence (F) of the pump beam, its power is measured and the fluence can then be determined using the formula $F = \frac{\text{Power}}{(\text{Spot size on sample})^2(\text{Laser Repetition Rate})}$. For our system this translates to $F\,(\text{mJ/cm}^2) = \frac{\text{Power (mW)}}{\pi(0.03\,\text{cm})^2(1000\,\text{Hz})}$. The system operates at a 1 kHz repetition rate. Due to the thickness of the sample we can assume that the laser light penetrates the whole sample[7].

We define the relative change in intensity as $\Delta I_{CDW}/I_{CDW}$, where $\Delta I_{CDW} = I_{CDW}(t) - I_{CDW}(t<0)$, which means that $\Delta I_{CDW}/I_{CDW}$ can have a value ranging from -1 to 0. Figure 6.1 shows a Bragg reflection and its satellite peaks at different time steps. At t=0.5 ps we see that there is a decrease in the intensity of the CDW peaks and at t=1 ps they vanish completely. In Figure 6.2 the relative change in intensity of the CDW ($\Delta I_{CDW}/I_{CDW}$) with time, following photoexcitation, is plotted. $\Delta I_{CDW}/I_{CDW}$ drops to -1 which means that the PLD is completely suppressed. This takes place on a timescale of less than 1 ps. In the images in Figure 6.1 there is no obvious change in the intensity of the Bragg peak, but plotting the relative change in intensity of the Bragg peaks ($\Delta I_{Bragg}/I_{Bragg}$), as shown in Figure 6.3, we see that there is a small change in intensity. Both these transient curves were obtained with a pump pulse fluence of 2.3 mJ/cm^2. The Bragg reflections undergo a much smaller change in intensity (an increase of less than 5 %) which means that the presence of the PLD in the CDW state decreases the efficiency of scattering into the Bragg peaks. As the CDW is destroyed, the Bragg reflections become brighter, but at the same time the lattice heats up. According to [8] this can be viewed as an effective Debye-Waller effect, which is observed by a decrease in the intensity of the Bragg reflections. At the applied fluence the total number of photons incident on the crystal of $(100\,\mu\text{m})^2$ is $\frac{2.3\times10^{-3}\,\text{J/cm}^2}{1.5\,\text{eV}}(100\,\mu\text{m})^2 \approx 10^{12}$. The number of unit cells in the crystal is $\frac{\text{volume(crystal)}}{\text{volume(unit cell)}} = \frac{30\,\text{nm}\times100\,\mu\text{m}\times100\,\mu\text{m}}{25\,\text{Å}\times3.5\,\text{Å}\times3.5\,\text{Å}} \approx 10^{12}$ which might indicate that the phase transition occurs once every unit cell absorbs one photon.

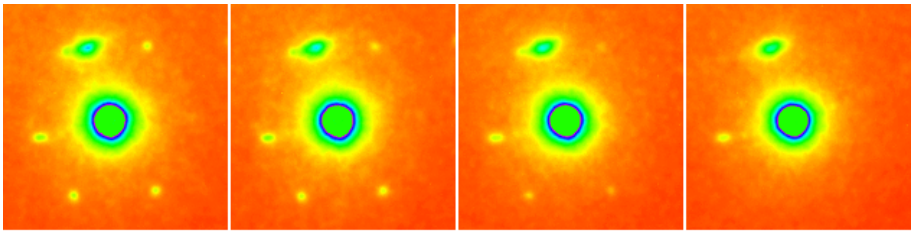

Figure 6.1: Temporal evolution of the intensity of the CDW superlattice with time. At 0.5 ps there is an obvious decrease in the intensity of the CDW peaks and at 1 ps they have vanished completely. The bright reflection at the top is probably a Bragg reflection from a neighbouring single crystal.

[7] There is no available literature to confirm this, but the optical penetration depth of light with a wavelength of 800 nm in 2H-$TaSe_2$ is $\gtrsim$100 nm [30], which was confirmed by absorption measurements.

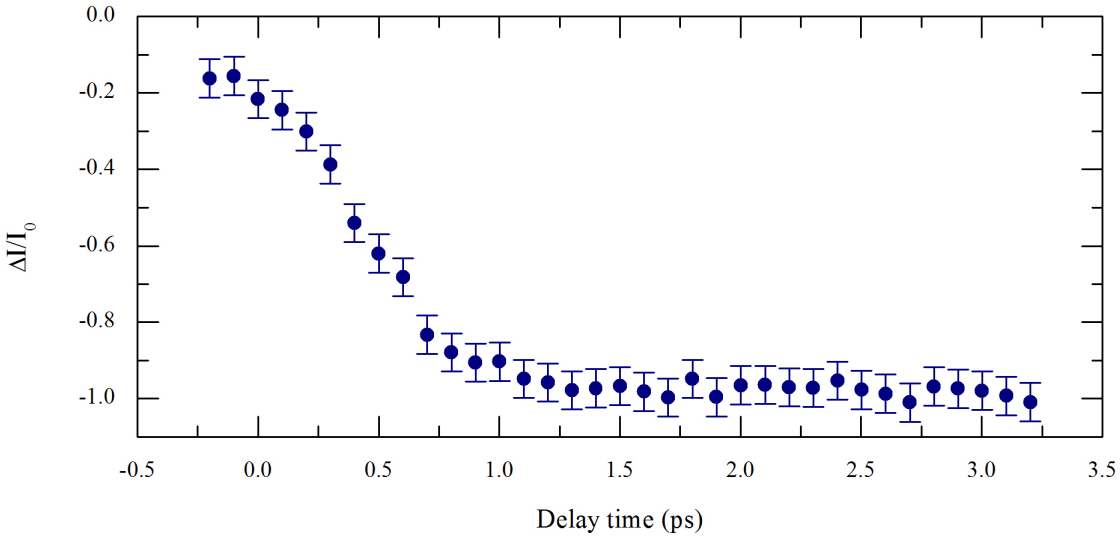

Figure 6.2: The transient curve for the CDW reflections showing the temporal evolution of the relative intensity of the superlattice after photoexcitation with a pump fluence of $2.3\,\mathrm{mJ/cm^2}$. The superstructure is completely suppressed in less than 1 ps. The indicated errors on the data points are retrieved from the scattering of the values around an expected smooth transient. The measurement was started slightly late, as can be seen in Figure 6.6.

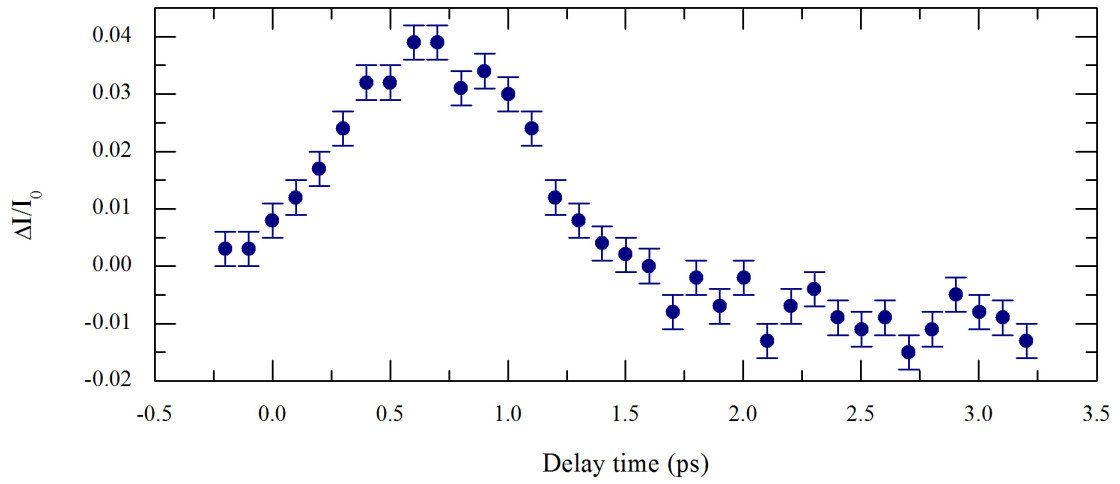

Figure 6.3: The transient curve for the Bragg reflections showing the temporal evolution of the relative Bragg intensity after photoexcitation with a pump fluence of $2.3\,\mathrm{mJ/cm^2}$. The Bragg reflection recovers within 1.5 ps.

I_{Bragg} recovers within 1.5 ps to its initial value, however for longer times it seems to be slightly smaller (values just below 0) in all measurements of strong CDW suppressions. This can be attributed to the combination of the increased scattering efficiency in the absence of the CDW and the decrease in scattering efficiency due to the lattice heating up. However, there is no sign of the recovery of the CDW in the first 3 ps. A scan over a longer period of time (see Figure 6.4) was done under the same conditions as in Figure 6.2, with a pump fluence of 2.3 mJ/cm^2, to determine the recovery time. A partial recovery to ∼-0.4 occurs within our temporal window of 1.7 ns. From this measurement we can estimate a time constant of 2 ns, but even longer scans are required to determine the actual time it takes for the sample to return to its initial state after energy is deposited into the system. From the fact that the signal $\Delta I_{CDW}/I_{CDW}$ is 0 at $t < 0$, we know that after 1 ms the CDW has fully recovered.

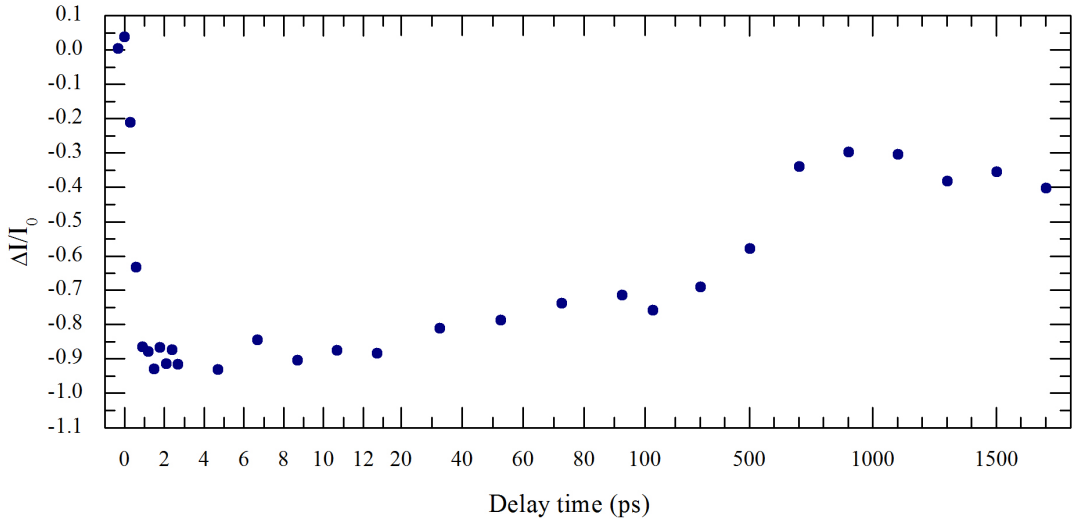

Figure 6.4: Long term recovery of the CDW after being pumped by a pulse with a fluence of 2.3 mJ/cm^2. Be aware of the three different time scales.

The temporal resolution of the measurement can be retrieved from the slope of the CDW trace under the assumption that the induced process is fast compared to the apparatus response, which is a convolution of the pump laser pulse duration and the electron pulse duration, and maybe temporal jitter between the pulses and the geometry of the setup. In Figure 6.5 the temporal evolution of I_{CDW} is plotted after being excited by a pump pulse with a fluence of 1.6 mJ/cm^2. The slope of the transient curve (the drop from 90% to 10%) can be used to estimate a temporal resolution of at least 400 fs which means that, assuming a laser pulse duration of 150 fs, the electron pulse duration is indeed in the order of 250 fs and that the overall jitter is very small.

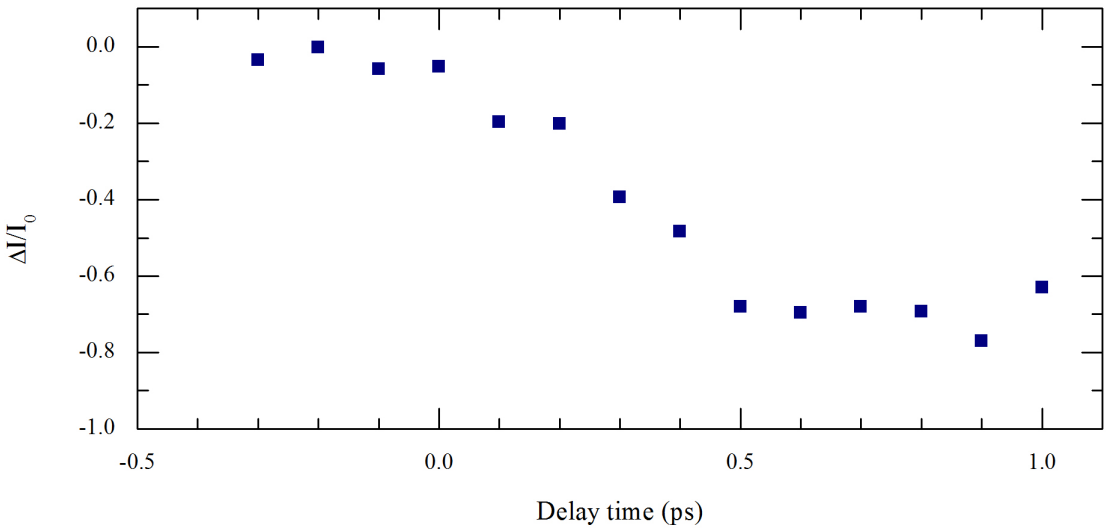

Figure 6.5: The change in the intensity of the CDW reflection after excitation with a pump pulse energy of 1.6 mJ/cm^2. From the slope of the cure the temporal resolution of the system can be extracted to be 400 fs.

The degree of suppression of the CDW and associated PLD depends on the fluence of the pump pulse. This can be seen in Figure 6.6 where $\Delta I_{CDW}/I_{CDW}$ is plotted for different excitation fluences. We found that a fluence of more than 2.2 mJ/cm^2 resulted in a complete suppression of I_{CDW} and for fluences of less than 1 mJ/cm^2 there is no observable change in the intensity of the superstructure. The complete disappearance of the CDW signature ($\Delta I_{CDW}/I_{CDW}$ = -1) indicates that the material has undergone a phase transition where the CDW is completely destroyed. A further hint in this direction is the long recovery time of a fully suppressed CDW: If the CDW is only perturbed, the superstructure (I_{CDW}) is still present, but its intensity is weaker. The recovery time is also influenced by the fluence of the pump pulse. For lower fluences there is a partial recovery on a few ps timescale, but for higher fluences there is no recovery within the first few ps plotted in the Figure 6.6. If the I_{CDW} drops to zero the system will likely need more time to recover to its original state. According to [29] this is due to the fact that if the CDW is only perturbed, the time needed by the sample to return to the original state only depends on the time it takes for the electronic system to shift energy to the lattice. If the CDW is destroyed, long-range structural correlations have to take place. Thus far we have not been able to do successful measurements on very long time scales for different degrees of suppression of the CDW. The relationship between the suppression of I_{CDW} and the fluence is plotted in Figure 6.7.

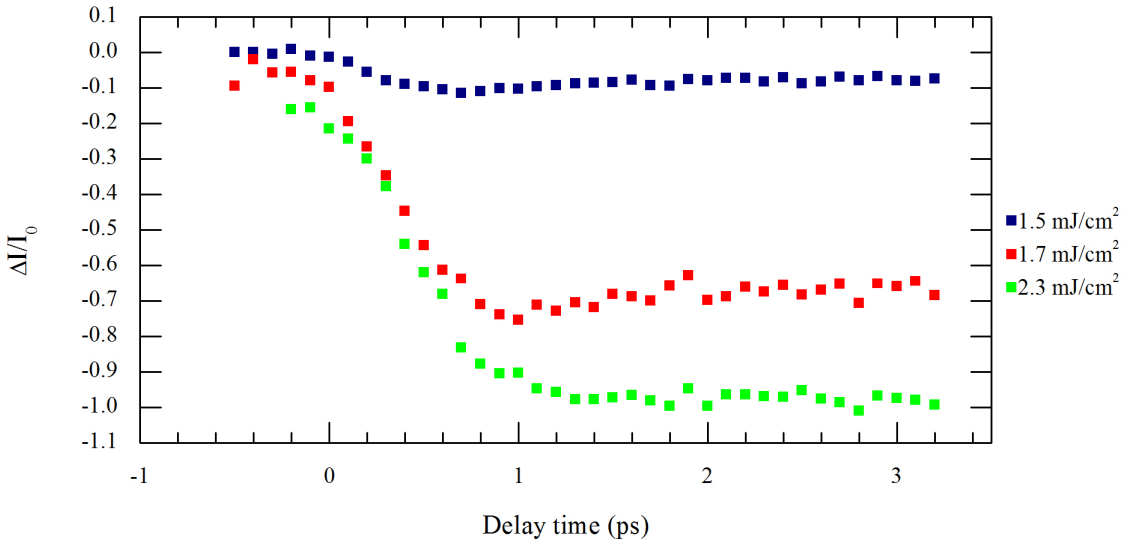

Figure 6.6: The suppression of I_{CDW} depends on the excitation fluence. If more energy is deposited into the system, the CDW is more perturbed and fluences $>2.2\,mJ/cm^2$ completely suppresses the CDW.

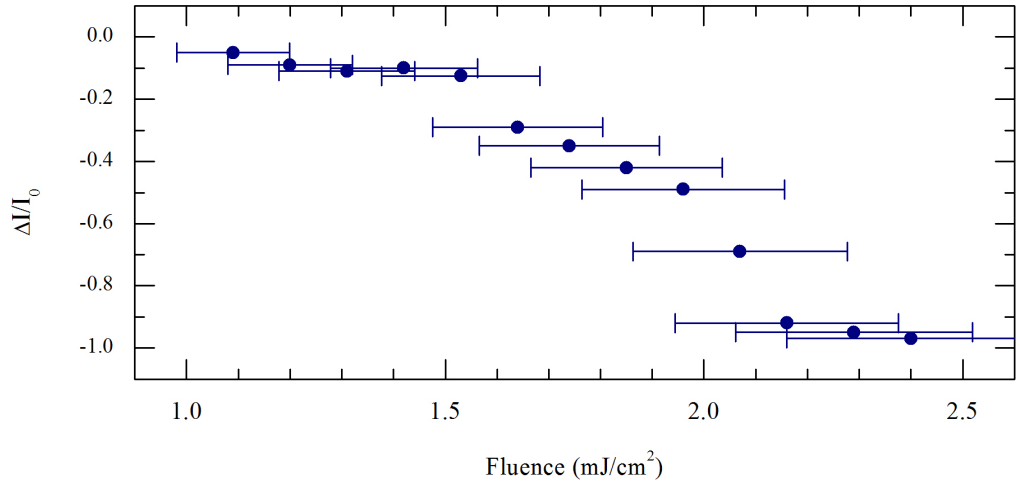

Figure 6.7: The relationship between the suppression of the charge density wave and the fluence of the pump pulse. The indicated errors of $\pm 10\%$ result from the fact that the power reading and the actual overlap might vary. We do not see this directly, but have noticed that a certain nominal flux does not always give the same level of CDW suppression. This measurement however, was done in one run over short time scales, under conditions which were kept constant as good as possible.

In Figure 6.8 a CDW transient curve for a lower pump fluence (1.5 mJ/cm^2) is plotted. The CDW is only suppressed by 10% and there is some recovery with a few ps. The very low signal to noise ratio means that we can even see changes as small as only a few percent with our system.

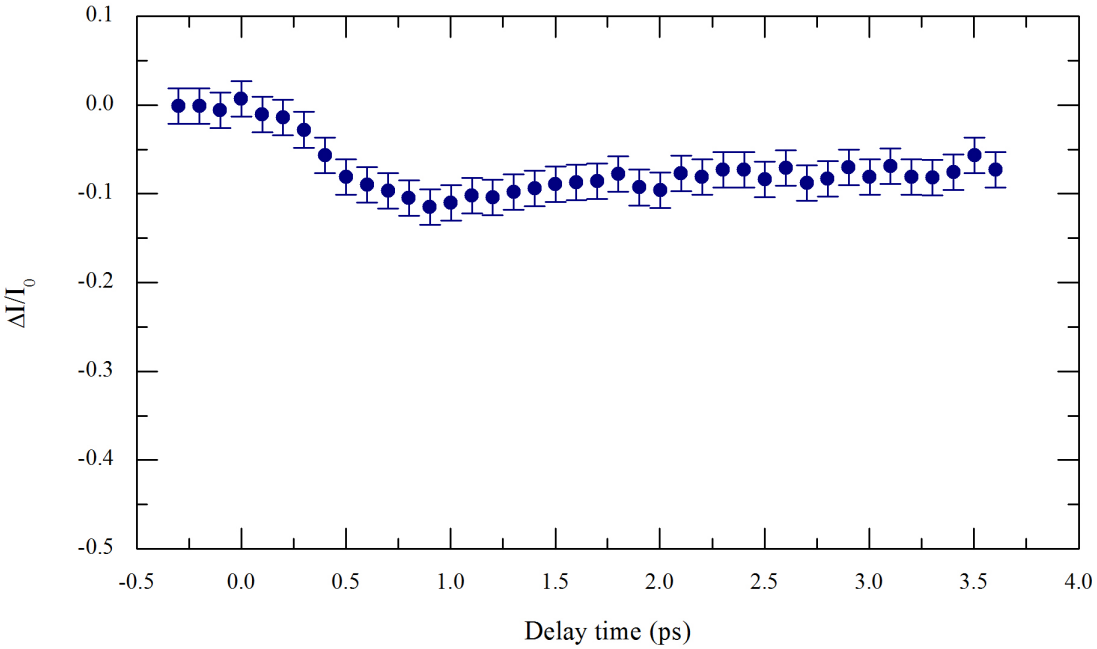

Figure 6.8: Suppression of the CDW with a 1.5 mJ/cm^{2}pump fluence. The signal to noise ratio is very low which means that small changes in the lattice can be seen with our system.

Observing the lattice after depositing energy into the system enabled us to see the suppression of the CDW (and the associated PLD) which takes place on a timescale of less than 1 ps. We were also able to establish a relationship between the suppression and the fluence of the pump pulse used to initiate this change. We saw that we can completely destroy the CDW by increasing the fluence and that the time needed to recover the CDW back to its initial state also depends on the fluence of the pump pulse. Our system has a low signal to noise ratio which enables us to observe very small changes in the lattice through ultrafast electron diffraction.

Part III

AN ALTERNATIVE SOURCE

Ultrafast electron diffraction is not the only method which can be used to obtain information on the structural dynamics in crystals. Time-resolved information about the atomic or molecular movement in crystals can also be acquired by replacing the electrons in the probe path of a pump-probe experiment by monochromatic, femtosecond X-ray pulses. At large synchrotron facilities pulsed X-rays are produced, but the pulse duration is in the order of 10–100 ps. By "slicing" out a small wedge of electrons from the electron bunch in the storage ring by modulating their energy using a femtosecond laser, ultra-short X-ray pulses (in the order of 100 fs) can be generated from synchrotron radiation [31, 32]. The new hard X-ray Free Electron Lasers produce bright, coherent, tunable X-rays with a pulse duration of 10–50 fs, but beam time at these large scale facilities is limited.

Ultra-short X-rays can also be generated in laboratories using a tabletop laser setup. This method is obviously not nearly as expensive as building a synchrotron, but unfortunately also not as efficient. Tabletop ultra-short X-rays can be produced through high harmonic generation [33] and by using laser-generated plasma sources [34]. In the following section I will discuss the second method and it is based on work done at the Westfälische Wilhelms-Universität in Münster, Germany. During my masters I spent five months there in the research group of Professor Helmut Zacharias, learning about laser plasma-based X-ray sources.

7 LASER PLASMA-BASED ULTRAFAST X-RAY SOURCE

The concept of laser plasma-based hard X-ray sources has been around for a long time. With the development of sub-picosecond lasers, the generation of laser plasma-based, ultra-short (< 1 ps) X-ray pulses became possible [35] and this lead to the first time-resolved X-ray diffraction experiments done on a sub-picosecond timescale [36]. Since then, ultra-short X-rays, produced by making use of high power, femtosecond laser sources, have been used to study structural dynamics in solids such as phase transitions [37] and the generation of optical and acoustic phonons [5]. The X-ray pulses are synchronised with the laser pulses due to the fact that they share the same source and an optical pump, X-ray probe setup can be used to obtain information on the structural dynamics in crystals.

The basic principle (illustrated in Figure 7.1) is as follows: A femtosecond laser with a high pulse energy and power is focused onto a solid target[8] and a plasma with solid state density is produced on the surface of the material. For laser pulses with about 100 fs duration and a 1 kHz repetition rate, a pulse energy of a few mJ is required. These pulses must be focused to intensities in the order of 10^{17} W/cm^2 in

[8] Solid-state targets include rotating disks, wires and moving tapes, but X-rays have also been generated through the use of liquid drop targets.

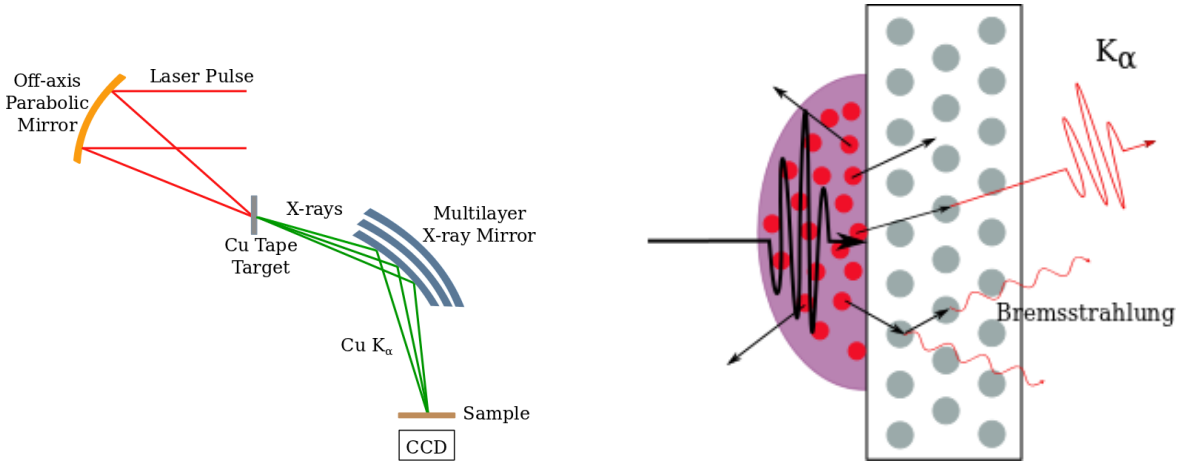

Figure 7.1: Schematic drawing of the generation of laser plasma-based X-rays (left) and the process which takes place at the target to produce characteristic X-rays and Bremsstrahlung (right).

order to generate a useful X-ray flux. Electrons from the plasma are accelerated (to energies in the range of 100 keV) into the target by the electric field of the laser light to produce characteristic X-ray lines by knocking out K-shell electrons and Bremsstrahlung through collisions. Due to the fact that the electric field of the laser light is responsible for the acceleration of the electrons into the target, it only happens while the light is present. This means that the pulse duration of each X-ray pulse depends on the laser pulse duration and the propagation time of the electrons through the metal, resulting in X-rays with a pulse duration similar to that of the femtosecond laser pulse used to generate the plasma. The emitted X-rays are collected and focused onto the sample using X-ray optics which, for example, can be dielectric coatings under grazing incidence on curved surfaces (typically ellipsoids) or toroidally bent Bragg mirrors. X-rays are generated isotropically in a 4π solid angle, but only a small part of the produced X-rays are utilised. The low flux and weak interaction of X-rays with matter means that normally only a single Bragg peak is monitored over the course of an experiment and not the entire diffraction pattern as is the case with ultrafast electron diffraction. An X-ray CCD camera is used as a detector and placed at the Bragg angle of reflection from a specific lattice plane for the particular K_α line.

Laser-plasma X-ray sources produce femtosecond X-rays with energies ranging from 1–25 keV at a repetition rate of 10 Hz to several kHz and are currently the only laboratory based sources which can produce ultra-short (femtosecond), hard X-rays [38]. The basic components needed to generate laser plasma-based ultra-short X-rays and do time resolved diffraction experiments are a high power, femtosecond laser, an appropriate target and X-ray optics to collect and focus the radiation. I will describe these different aspects of the ultrafast X-ray diffraction experiment in Münster.

The laser system (refer to Figure 7.2) consists of a commercial Ti:sapphire oscillator/amplifier system (*Femtosource PRO/OMEGA 1000*) which produces pulses with a wavelength of 800 nm and a pulse energy

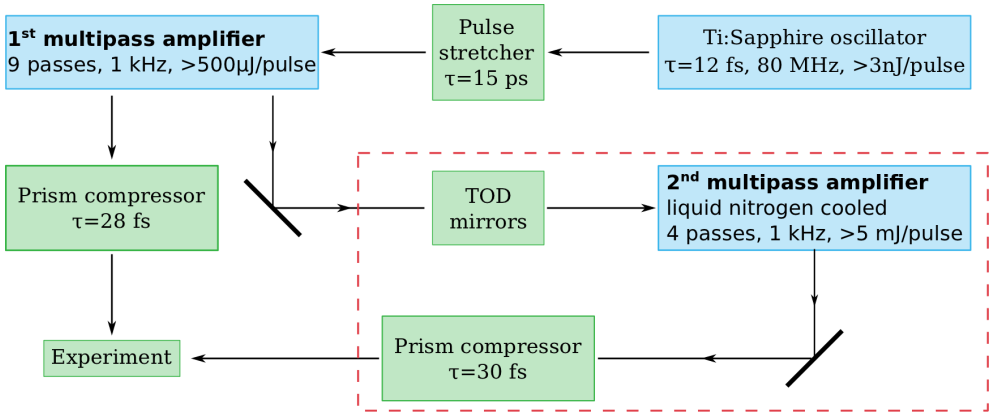

Figure 7.2: To produce ultra-short X-rays a femtosecond laser with high pulse energies is required. The X-ray flux can be increased by having more power and therefore the laser system has two amplifiers to push the pulse energy up to 5 mJ.

of $> 500\,\mu$J at a repetition rate of 1 kHz. After compression in a prism compressor a pulse duration of 28 fs can be achieved, but to generate a sufficient flux of hard X-rays, a higher pulse energy is required and therefore the system contains a second multipass amplifier (4-pass cryogenic CPA system) into which the light from the first amplifier is coupled. In the second amplification stage the beam makes four passes through a Brewster-cut Ti:sapphire crystal. To prevent thermal lensing, the crystal is cooled with liquid nitrogen to 120 K, but it has to be kept under vacuum to avoid condensation on the crystal. After the second amplification the beam goes through a prism compressor (consisting of two Homosil prism sequences) and pulses with a wavelength of 800 nm, a pulse duration of 30 fs and a pulse energy of more than 5 mJ can be obtained at a 1 kHz repetition rate.

The generation of X-rays has to take place in vacuum. The reason for this is to prevent the formation of a plasma in air and to ensure that a plasma is produced on the surface of the target. Therefore a vacuum of anything less than 1 mbar is sufficient. The laser beam is expanded (to a beam diameter of 40 mm), enters the chamber through an entrance window and is directed onto a gold coated off-axis parabolic mirror which focuses it onto the moving target. A parabolic mirror is used because there is no spherical or chromatic aberration and the diameter of the focal spot is 5 μm. The alignment of such a mirror is quite sensitive and therefore it is mounted on a micrometer translation stage to enable fine adjustment to ensure that the focus is on the target. The target is a Cu film with a thickness of 12.5 μm which can be moved at different speeds to ensure that a new part of the tape target is exposed to every laser pulse (see the illustration of the vacuum chamber in Figure 7.3). A debris band, mounted on a rotating axis, runs around the target tape to protect the parabolic mirror and the X-ray optics from debris which is produced by the interaction of the laser light with the metal tape. The tape is transparent to the laser light and X-rays and is also kept moving to prevent the buildup of debris.

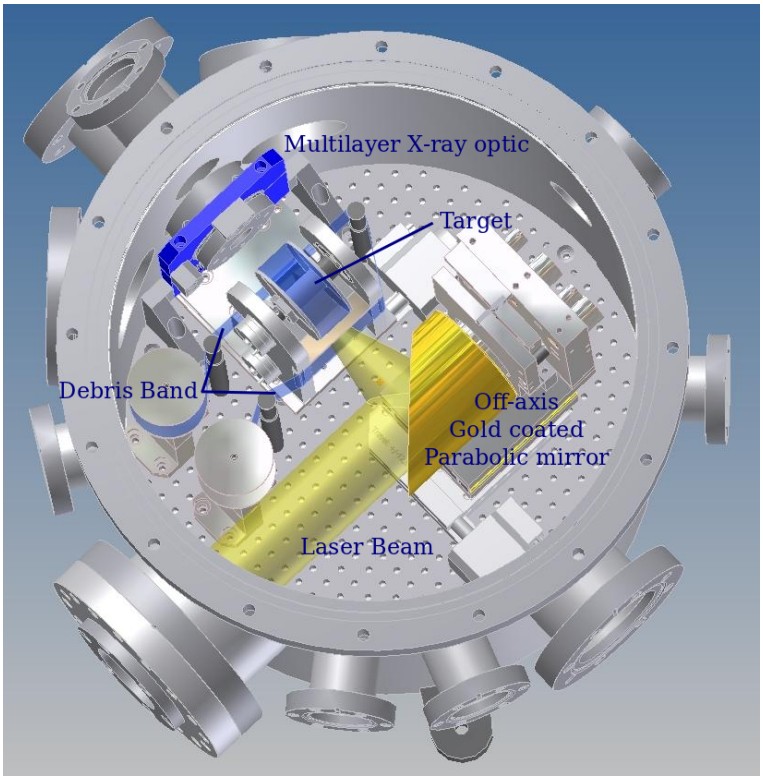

Figure 7.3: The design of the vacuum chamber where the X-rays are generated, showing the different components of the system.

The X-rays which are produced are the characteristic lines of Cu (Cu-K_α radiation with an energy of 8.05 keV an Cu-K_β at 8.9 keV) on a background of Bremsstrahlung. X-rays are produced in a 4π solid angle, but in order to do diffraction experiments they need to be collected and focused. This is done by a multilayer mirror (Ni/B_4C) which is used to guide the X-rays, but also acts as a spectral filter, specifically designed for Cu-K_α radiation. It consists of 5 elliptical mirrors which can focus the X-rays down to a spot size of 500 μm. The mirrors are already fixed at the correct angles with respect to each other, which makes the alignment easier, but it is still a delicate process. The focal lengths are 100 mm and 500 mm which means that the X-ray source has to be exactly 100 mm from the optic. It is also necessary to have the source and the sample on the same optical axis as that of the optic. The fact that the X-rays cannot be seen by eye and an image (with an exposure time which can be in the order of minutes) has to be acquired to view the focus, also complicates things. The optic is housed in a casing (see Figure 7.4) and can be adjusted by a picomotor controller (*Newport iPico MCL 8752*) which is operated from outside the chamber.

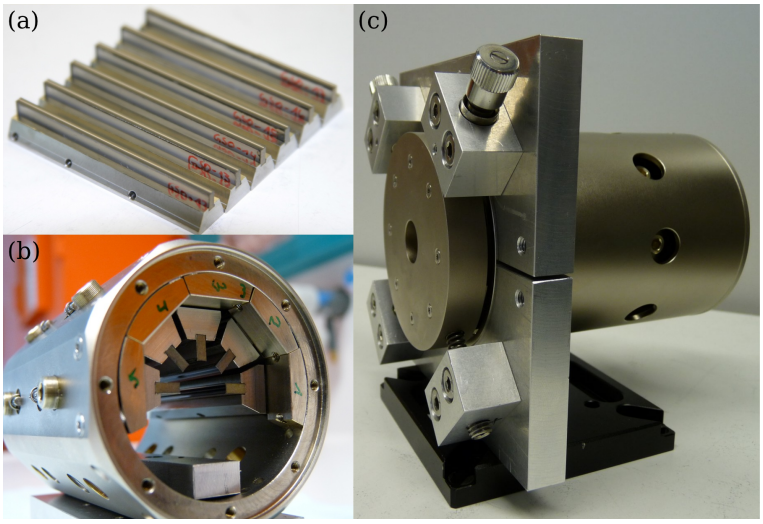

Figure 7.4: The Multilayer (Ni/B_4C) X-ray Mirror. Panel (a) shows the 5 elliptical mirrors and in (b) they are mounted at the appropriate angles with respect to each other. In (c) the complete mirror mount is shown with the picomotor screws visible.

A spectrum of the X-rays generated by a laser plasma-based system with a Ti target is shown in Figure 7.5. It shows a clear Ti-K_α peak at 4.51 keV with a smaller Ti-K_β peak at 4.9 keV. It is not shown in this spectrum, but usually there will be two additional bumps at 9.02 keV and 9.8 keV which occur when two K_α or K_β photons with the same energy are detected simultaneously and this is referred to as the pileup.

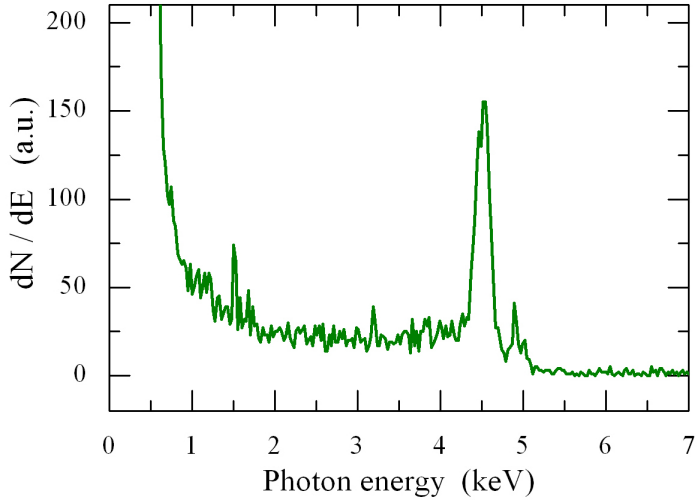

Figure 7.5: A generated X-ray spectrum showing a strong peak at 4.51 keV (Ti-K_α) and a smaller peak at 4.9 keV (Ti-K_β). Data taken from [39].

Laser plasma-based ultrafast X-ray pulses are useful because they are the only laboratory source of ultra-short, hard X-ray radiation. The energies are well-defined and a pulse duration of a few hundred femtoseconds can be achieved. The downside is that the flux is very low and experiments need to run for extended periods of time to obtain sufficient information. In the order of 10^{10} Cu-K_α photons per second are generated, but as already said this is in a 4π solid angle and X-ray optics only cover a solid angle of 10^{-4} which means that, if the reflectivity of the mirror is ~ 1, 10^6 photons per second fall in on the target. This sounds like a lot compared to electron diffraction where we have only 10^4 electrons per second on the target, but electrons have a 10^5 times higher scattering cross section than X-rays. Nonetheless, successful experiments [5, 36, 37] have been done using laser plasma-based ultrafast X-ray diffraction to obtain valuable information on the structural dynamics in crystals.

8 CONCLUSION

Ultrafast electron diffraction (UED) has been proven to be a compact and powerful tool to investigate photoinduced structural dynamics which take place in crystalline samples on a sub-picosecond timescale. Utilising the pump-probe technique, it offers complementary information to ultrafast structural studies done with X-rays at large scale synchrotron facilities and free electron lasers, but the difference in scale and availability between these methods has lead to an increase in the use of UED sources. More complicated samples are being investigated with UED, but the number of laboratories obtaining results is still below ten.

In order to bring the UED system at the University of Stellenbosch to the level of the leading UED laboratories in the world and where experiments can be done, required some improvements to be made. These included improving the performance of the photocathode and the detection of electron diffraction patterns, as well as setting techniques in place to obtain spatial and temporal overlap and to determine the properties of the electron beam. The characterisation of the electron beam includes determining the number of electrons, the beam size and the electron pulse duration. It was also necessary to develop software and methods to run experiments over periods as long as 20 hours, without losing spatial and temporal overlap and with monitoring the overall stability of the setup and the laboratory. Another important technique which had to be learnt was the preparation of thin samples (< 100 nm thick) which are required for electron diffraction experiments in transmission geometry. All of these techniques and improvements are discussed in this thesis.

The next step was to do actual experiments to prove the functionality of the system. For this we needed a sample which is thin, crystalline and undergoes a photoinduced structural change at room temperature from which it recovers to its initial state within less than 1 ms, because the system operates at a 1 kHz repetition rate. These requirements were met by the transition-metal dichalcogenide $4H_b$-$TaSe_2$. The properties (including the structure and different phases) of the sample are described, but before doing experiments it is necessary to understand what information can be obtained from electron diffraction patterns. For this reason an overview of electron diffraction theory and how to extract information from an electron diffraction pattern is given. This is followed by a summary of the data analysis procedure.

With all these elements in place, the first time-resolved ultrafast electron diffraction experiments were done on $4H_b$-$TaSe_2$. The suppression of the charge density wave (CDW) was observed by monitoring the associated periodic lattice distortion (PLD). The degree of suppression depends on the amount of energy deposited into the system (meaning the fluence of the pump pulse) and takes place on a time scale of less than 1 ps. A relationship between the fluence of the pump pulse and the change in intensity of the CDW reflection was established and the estimated recovery time if the CDW is completely destroyed, is 7 ns.

UED is not the only laboratory-based method by which the atomic motion in crystals can be monitored and for this reason an alternative source, namely ultrafast laser plasma-based X-rays, is discussed.

The $TaSe_2$-experiments have proven that the system functions and that structural dynamics can be

observed on sub-picosecond time scales. The system was improved to the point where the obtained results can be trusted and the next step is to investigate more complicated samples. Future plans include the study of another transition-metal dichalcogenide, namely 1T-$TiSe_2$, which undergoes a phase transition at 202 K. For this, a cooling system is in the process of being incorporated into the setup. Another interesting material which is the organic molecular radical ion crystal Cu(dicyanoquinonediimine)$_2$ which undergoes a photoinduced insulator-to-conductor phase transition, accompanied by a structural change and a change in the volume of the unit cell. These are just a few of many samples with interesting properties which can be studied with UED. Seeing that UED is a fairly new method, many exciting results will still come from this field.

References

[1] M. von Laue, *Röntgenstrahlinterferenzen*, Physikalische Zeitschrift **14**, 1075 (1913)

[2] C. Davisson and L. H. Germer, *Diffraction of Electrons by a Crystal of Nickel,* Physical Review **30**, 705 (1927)

[3] E. O. Wollan and C. G. Shull, *The Diffraction of Neutrons by Crystalline Powders*, Physics Review **78**, 830 (1948)

[4] J. Miao, K. O. Hodgson, T. Ishikawa, C. A. Larabell, M. A. LeGros and Y. Nishino, *Imaging whole Escherichia coli bacteria by using single-particle X-ray diffraction*, Proc. Natl. Acad. Sci. **100**, 110 (2003)

[5] K. Sokolowski-Tinten, C. Blome, J. Blums, A. Cavalleri, C. Dietrich, A. Tarasevitch, I. Uschmann, E. Förster, M. Kammlers, M. Horn-von-Hoegen and D. von der Linde, *Femtosecond X-ray measurement of coherent lattice vibrations near the Lindemann stability limit*, Nature **422**, 287 (2003)

[6] J. B. Siwick, J. R. Dwyer, R. E. Jordan and R. J. D. Miller, *An Atomic-Level View of Melting Using Femtosecond Electron Diffraction*, Science **302**, 1382 (2003)

[7] P. Baum, D. Yang and A. H. Zewail, *4D Visualization of Transitional Structures in Phase Transformations by Electron Diffraction*, Science **318**, 788 (2007)

[8] M. Eichberger, H. Schäfer, M. Krumova, M. Beyer, J. Demsar, H. Berger, G. Moriena, G. Sciaini and R. J. D. Miller*, Snapshots of cooperative atomic motions in the optical suppression of charge density waves,* Nature **468**, 799 (2010)

[9] K. Tiedtke *et al.*, *The soft X-ray free-electron laser FLASH at DESY: Beamlines, diagnostics and end-stations*, New Journal of Physics **11**, 023029 (2009)

[10] J. Cao, Z. Hao, H. Park, C. Tao, D. Kau and L. Blaszczyk, *Femtosecond electron diffraction for direct measurement of ultrafast atomic motions,* Applied Physics Letters **83**, 1044 (2003)

[11] Nicolas Erasmus, *The development of an electron gun for performing ultrafast electron diffraction experiments*, MSc Thesis, Stellenbosch University, 2009.

[12] M. J. Berger and S. M. Seltzer, *Tables of energy-losses and ranges of electrons and positrons*, NASA SP-3012, 1964.

[13] G. H. Kassier, K. Haupt, N. Erasmus, E. G. Rohwer, H. M. von Bermann, H. Schwoerer, S. M. M. Coelho and F. D. Auret, *A compact streak camera for 150 fs time resolved measurement of bright pulses in ultrafast electron diffraction,* Rev. Sci. Instrum. **81**, 105103 (2010).

[14] Günther H. Kassier, *Ultrafast electron diffraction: Source development, diffractometer design and pulse characterisation,* PhD Dissertation, Stellenbosch University, 2010.

[15] C. T. Hebeisen, G. Sciaini, M. Harb, R. Ernstorfer, T. Dartigalongue, S. G. Kruglik and R. J. D. Miller, *Grating enhanced ponderomotive scattering for visualization and full characterization of femtosecond electron pulses,* Optics Express **16**, 3334 (2008)

[16] N. Reid, *Ultramicrotomy, 4th ed.*, Elsevier, 1980.

[17] David B. Williams and C. Barry Carter, *Transmission Electron Microscopy: A Textbook for Materials Science, 2nd ed.*, Springer, 2009.

[18] J. A. Wilson and S. Di Salvo and F. J. Mahajan, *Charge-density waves and superlattices in metallic layered transition-metal dichalcogenides*, Advances in Physics **24**, 117 (1975)

[19] K. Rossnagel, *On the origin of charge-density waves in select layered transition-metal dichalcogenides,* Journal of Physics: Condensed Matter **23**, 213001 (2011)

[20] E. Bjerkelund and A. Kjekshus, *On the Structural Properties of the $Ta_{1+x}Se_2$ Phase*, Acta Chemica Scandinavica **21**, 513 (1967)

[21] R. E. Thorne, *Charge-density-wave conductors*, Physics Today, **49**, 42 (1996)

[22] R. Moret and E. Tronc, *CDW Induced Atomic Shifts in $4H_b$-$TaSe_2$*, Physica **99B**, 56 (1980)

[23] J. Ludecke, S. van Smaalen, A. Spijkerman, J. L. de Boer and G. A. Wiegers, *Commensurately modulated structure of $4H_b$ -$TaSe_2$ determined by x-ray crystal-structure refinement,* Physical Review B **59**, 6063 (1999)

[24] B. E. Brown and D. J. Beerntsen, *Layer Structure Polytypism Among Nobium and Tantalum Selenides*, Acta Crystallographica **18**, 31 (1965)

[25] Louis de Broglie, *Recherches sur la théorie des quanta*, PhD Dissertation, 1924.

[26] B. E. Beeston, *Electron Diffraction and Optical Diffraction Techniques*, Elsevier Science Ltd, 1994.

[27] W. Massa, *Crystal Structure Determination*, Springer, 2000

[28] F. J. Di Salvo, D. E. Moncton, J. A. Wilson and S. Mahajan, *Coexistence of two charge-density waves of different symmetry in 4Hb-TaSe2*, Physical Review B **14**, 1543 (1976)

[29] E. Möhr-Vorobeva, S. L. Johnson, P. Beaud, U. Staub, R. De Souza, C. Milne, G. Ingold, J. Demsar, H. Schäfer and A. Titov, *Nonthermal Melting of a Charge Density Wave in $TiSe_2$,* Physical Review Letters **107**, 036403 (2011)

[30] J. Demsar, L. Forró, H. Berger and D. Mihailovic, *Femtosecond snapshots of gap-forming charge-density-wave correlations in quasi-two-dimensional dichalcogenides 1T-TaS_2 and 2H-$TaSe_2$*, Physical Review B **66**, 041101 (2002)

[31] A. A. Zholents and M. S. Zolotorev, *Femtosecond X-Ray Pulses of Synchrotron Radiation*, Physical Review Letters **76**, 912 (1996)

[32] R. W. Schoenlein, S. Chattopadhyay, H. H. W. Chong, T. E. Glover, P. A. Heimann, C. V. Shank, A. A. Zholents and M. S. Zolotorev, *Generation of Femtosecond Pulses of Synchrotron Radiation*, Science **287**, 2237 (2000)

[33] Z. Chang, A. Rundquist, H. Wang, M. M. Murnane and H. C. Kapteyn, *Generation of Coherent Soft X-rays at 2.7nm Using High Harmonics*, Physical Review Letters **79**, 2967 (1997)

[34] J. Kutzner, M. Silies, T. Witting, G. Tsilimis and H. Zacharias, *Efficient high-repetition-rate fs-laser based X-ray source*, Applied Physics B **78**, 949 (2004)

[35] M. M. Murnane, H. C. Kapteyn, M. D. Rosen and R. W. Falcone, *Ultrafast X-ray Pulses from Laser-Produced Plasmas,* Science **251**, 531 (1991).

[36] C. Rischel, A. Rousse, I. Uschmann, P. A. Albouy, J. P. Geindres, P. Audebert, J. C. Gauthier, E. Förster, J. L. Martin and A. Antonetti, *Femtosecond time-resolved X-ray diffraction from laser-heated organic films,* Nature **390**, 490 (1997)

[37] C. W. Siders, A. Cavalleri, K. Sokolowski-Tinten, Cs. Tóth, T. Guo, M. Kammler, M. Horn von Hoegen, K. R. Wilson, D. von der Linde and C. P. J. Barty, *Detection of Nonthermal, Melting by Ultrafast X-ray Diffraction*, Science **286**, 1340 (1999)

[38] M. Chergui and A. H. Zewail, *Electron and X-Ray Methods of Ultrafast Structural Dynamics: Advances and Applications*, ChemPhysChem **10**, 28 (2009)

[39] F. Ewald, H. Schwoerer and R. Sauerbrey, K_α*-radiation from relativistic laser-produced plasmas,* Europhysics Letters **60,** 710 (2002)